Gondwana Research 79 (2020) 140–156

Contents lists available at ScienceDirect

Gondwana Research

journal homepage: www.elsevier.com/locate/gr

Evidence for southward subduction of the Mongol-Okhotsk oceanic plate: Implications from Mesozoic adakitic lavas from Mongolia

Thomas C. Sheldrick [a, *], Tiffany L. Barry [a], Ian L. Millar [b], Dan N. Barfod [c], Alison M. Halton [d], Dan J. Smith [a]

[a] School of Geography, Geology and the Environment, University of Leicester, University Road, Leicester, LE1 7RH, UK
[b] NERC Isotope Geosciences Laboratory, Keyworth, Nottingham, NG12 5GG, UK
[c] NERC Argon Isotope Facility, Scottish Universities Environmental Research Centre, Scottish Enterprise Technology Park, East Kilbride, G75 0QF, UK
[d] School of Physical Sciences, The Open University, Walton Hall, Milton Keynes, MK7 6AA, UK

ARTICLE INFO

Article history:
Received 25 February 2019
Received in revised form
6 September 2019
Accepted 6 September 2019
Available online 9 October 2019

Keywords:
Adaatsag/Ereendavaa terrane
Middle gobi volcanic belt
Central Asian orogenic belt
Double-sided subduction
Sr-Nd-Pb-Hf isotopes

ABSTRACT

A combination of new $^{40}Ar/^{39}Ar$ dating results, major- and trace-element data, plus Sr-Nd-Pb-Hf isotope data, are used to investigate the petrogenesis of Triassic high-Si adakite (HSA), Cretaceous low-Si adakite-like (LSA) lavas, and Cretaceous high-K and shoshonitic trachyandesite lavas, from eastern and south-central Mongolia. All samples are light rare-earth element and large-ion lithophile element enriched but depleted in some high-field strength elements (notably Nb, Ta and Ti). Two alternative models are proposed to explain the petrogenesis of the HSA samples. (1) A southward-subducting Mongol-Okhotsk slab underwent partial melting in the Triassic during the closure of the Mongol-Okhotsk Ocean, with the resultant melts assimilating mantle and crustal material. Alternatively (2), a basaltic underplate of thickened (>50 km; >1.5 GPa), eclogitic lower crust foundered into the underlying mantle, and underwent partial melting with minor contamination from mantle material and some shallow-level crustal contamination. The LSA samples are interpreted as melts derived from a lithospheric mantle wedge that was previously metasomatised by slab melts. Similarly, the trachyandesite lavas are interpreted as melts deriving from a subduction-enriched subcontinental lithospheric mantle. The spatial distribution of these samples implies that metasomatism likely occurred due to a southward-subducting Mongol-Okhotsk slab associated with the closure of the Mongol-Okhotsk Ocean. When this interpretation is combined with previous evidence for a northward-subducting Mongol-Okhotsk slab it advocates that the Mongol-Okhotsk Ocean closed with double-sided subduction.

1. Introduction

Far East Russia, central Mongolia and NE China form part of the Central Asian Orogenic Belt (CAOB), located between the Siberian Craton to the north, and the Tarim and North China Craton to the south, and extends for >4000 km from the Tian Shan of Central Asia in the west, to the Sea of Okhotsk in the east (e.g., Windley et al., 2007; Rippington et al., 2008, 2013; Zhou et al., 2010; Zhou and Wilde, 2013; Safonova and Santosh., 2014; Xiao et al., 2015; Safonova, 2017). Although the Paleozoic tectonic evolution of NE China was dominated by the amalgamation of microcontinental massifs and the closure of the Paleo-Asian Ocean (e.g., Sengör et al., 1993; Sengör and Natal'in, 1996), the Mesozoic tectonic evolution of East Russia, central Mongolia and NE China was largely influenced by Paleo-Pacific and Mongol-Okhotsk tectonic systems (e.g., Tang et al., 2014; Dash et al., 2015). Thus, the CAOB is a large and complex accretionary orogenic belt, influenced by the closure of multiple oceans.

The Mongol-Okhotsk suture (Fig. 1) comprises of ophiolites (Zonenshain et al., 1990; Tomurtogoo et al., 2005) and sediments containing marine fossils (Halim et al., 1998), attesting to the existence of the Mongol-Okhotsk Ocean (e.g., Seton et al., 2012). However, how and when the Mongol-Okhotsk Ocean closed is still a matter of debate despite being integral to unravelling the geological complexities of the CAOB (e.g., Bussien et al., 2011; Ruppen et al., 2014; Fritzell et al., 2016; Liang et al., 2019). This ocean formed in the Carboniferous between the continental blocks of Siberia to the north and Amuria (Mongolia)–North China blocks to the south

* Corresponding author.
E-mail address: ThomasSheldrick@gmail.com (T.C. Sheldrick).

https://doi.org/10.1016/j.gr.2019.09.007

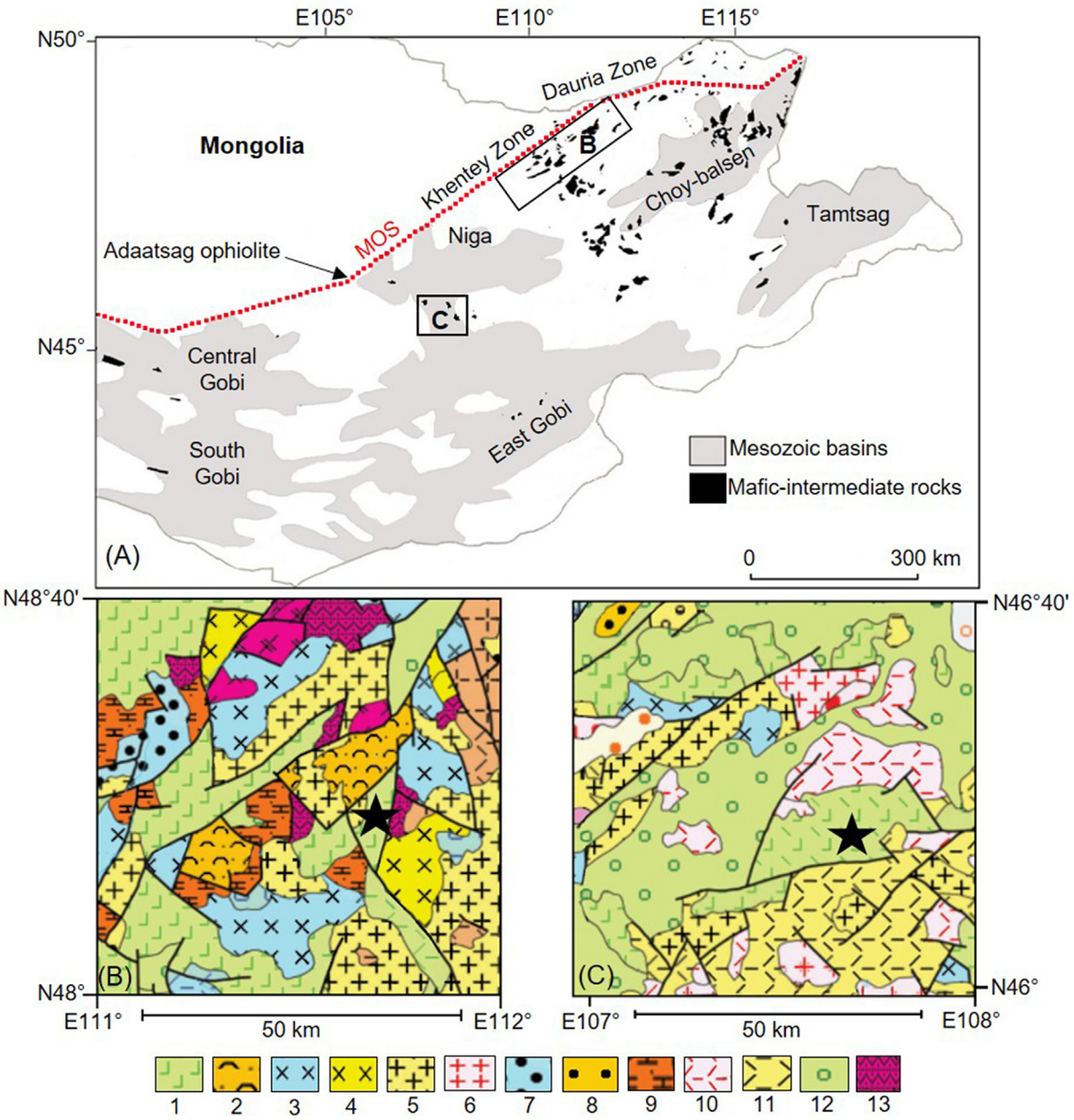

Fig. 1. A sketch map of Mongolia showing the sample areas and the distribution of Mesozoic mafic to intermediate volcanism south of the Mongol-Okhotsk suture (MOS). Sample areas: (B) low-Si adakite and Group 1 samples and (C), high-Si adakite and Group 2 samples. The distribution of volcanism is based on Mongolian government geological maps and field observations. The distribution of Mesozoic sedimentary basins is from Johnson et al. (2003). Two small insert geological maps from Tomurtogoo, 1999 show the surrounding geology next to the low-Si adakite (Map B) and high-Si adakite (Map C) localities (black stars). Insert maps key: 1, basalt and basalt-andesite formations; 2, tufogenic-terrigenous formations; 3–6, granite-granodiorite formations; 7–8, terrigenous sediment; 9, carbonate-terrigenous formation; 10–11, rhyolite; 12, coal-bearing molasse; and 13, poly-metamorphic complex.

(e.g., Tomurtogoo et al., 2005; Cocks and Torsvik, 2007; Van der Voo et al., 2015). The final closure time of the Mongol-Okhotsk Ocean is estimated to have occurred sometime between the Late Jurassic (~155 Ma) and the beginning of the Early Cretaceous (~120 Ma) and intrusions and marine fossils found in the Mongol-Okhotsk suture young from west to east, suggesting that the ocean closure started in the west and ended in the east (e.g., Zonenshain et al., 1990; Halim et al., 1998; Kravchinsky et al., 2002; Tomurtogoo et al., 2005; Van der Voo et al., 2015). However, there is uncertainty whether this ocean closed with double-sided subduction, or whether there was subduction along the northern, or southern margin only (e.g., Windley et al., 2010; Bussien et al., 2011; Wang et al., 2015; Van der Voo et al., 2015; Fritzell et al., 2016). Evidence for northwards subduction of the Mongol-Okhotsk oceanic plate includes arc-related calc-alkaline granodiorites, granites and quartz diorites (Zorin, 1999) in the Khentey and Dauria zones (Fig. 1), seismic tomographic images of slabs (Van der Voo et al., 1999); detrital zircon analysis studies from the Hangai – Khentey basin (Badarch et al., 2002; Kelty et al., 2008; Bussien et al., 2011) and numerical modelling results (Fritzell et al., 2016). However, zircon analysis studies, on samples from the Ereendavaa terrane and Middle Gobi volcanic belt, south of the Mongol-Okhotsk suture, suggest that there was also subduction on the southern margin and indicate that the final suturing of the Mongol-Okhotsk Ocean occurred after the Triassic (Bussien et al., 2011). Nevertheless, some models have advocated for northward or southward subduction only (e.g., Meng,

2003; Seton et al., 2012; Bars et al., 2018). This lack in understanding leads to difficulties in reconstructing the history and geometry of this penultimate ocean closure event which united the Asian continent.

The North China Craton and southern Mongolia underwent widespread removal of lithospheric mantle in the Mesozoic (e.g., Gao et al., 2002; Zhang et al., 2002; Menzies et al., 2007; Sheldrick et al., 2018). Yet little is understood as to whether the closure of the Mongol-Okhotsk Ocean influenced Mesozoic magmatic and/or lithospheric removal processes; for example, Bars et al. (2018) concluded that Mesozoic magmatism across southern Mongolia and the North China Craton was due to Paleo-Pacific slab roll-back rather than from any involvement of a southward-subducting Mongol-Okhotsk ocean plate. Other researchers have attributed double-sided subduction to facilitating Mesozoic magmatic processes in southern Mongolia (e.g., Windley et al., 2010; Sheldrick et al., 2018; Tang et al., 2018). In the North China Craton, voluminous granitoid magmatism has been attributed to southward subduction of the Mongol-Okhotsk Plate (Liu et al., 2018; Dai et al., 2019; Zhao et al., 2019), while a slab window model, for the genesis of volcanism in the Great Xing'an Range, was suggested by Zhang (2014). Recent research from Deng et al. (2019) also proposes that flat-slab subduction of the Mongol-Okhotsk oceanic plate might explain magmatism in the Great Xing'an Range and contemporaneous foreland folding and thrusting. Furthermore, such large-scale models invoking southward subduction of the Mongol-Okhotsk oceanic plate could have had implications for asthenospheric flow (e.g., Barry et al., 2017) and may have facilitated convective erosion of the lithosphere (e.g., He, 2014, 2015).

To investigate whether an oceanic slab was subducted southwards beneath southern Mongolia and potentially northern China, we examine two occurrences of adakitic lavas from south of the Mongol-Okhotsk suture and compare them to nearby Mesozoic lavas (Fig. 1). The term "adakite" has caused unnecessary confusion in the literature, because adakites are often interpreted to be partial melts of subducted basalt which has been metamorphosed to eclogite or amphibolite only (Castillo, 2006). However, adakite geochemical signatures can be generated from a variety of processes, such as melting of underplated lower crust (Atherton and Petford, 1993), delamination of lower crust (Xu et al., 2002) and fractional crystallisation of late stage accessory minerals such as apatite (Moyen, 2009). Traditionally rock classifications are based on mineralogy/geochemistry rather than melting process or source (e.g., Winchester and Floyd, 1977), and we suggest that this is the best approach. Herein, we classify our samples as adakite/adakitic based on major- and trace-element geochemistry alone (Defant and Drummond, 1990; Castillo, 2006): low MgO (<3 wt %), high Al_2O_3 (>15 wt %), high SiO_2 (>56 wt %), high Sr (>300 ppm), low Yb (<1.9 ppm) and high La/Yb (>20).

2. Geological setting

Low-silica adakite (LSA) samples (TCS 7.1 to TCS 7.7) were collected from a large outcrop on the border of the Adaatsag and Ereendavaa terrane (Fig. 1). The Adaatsag terrane, which extends into northeast Russia, is described as an accretionary wedge (Badarch et al., 2002) and represents part of the Mongol-Okhotsk Belt; a part of the Mongol-Okhotsk suture. As described by Badarch (2005), the Adaatsag terrane contains serpentinized dunites and harzburgites associated with Carboniferous layered gabbro, sheeted mafic dykes, basalts overlain by red cherts and clastic sediments, suggesting an evolved ocean crust existed within the Carboniferous. The adjacent Ereendavaa terrane extends into Russia and NE China and is a cratonic terrane that includes plutonic granite intrusions as young as Lower Jurassic (Badarch et al., 2002). Samples TCS 7.1 to 7.7 represent different units through a sequence of lavas; where TCS 7.1 was at the top and TCS 7.7 at the base, of the sequence. Trachyandesite and trachyte lavas (TCS 2.1 to 13.1; Group 1) were also collected from the area around the LSA outcrop (~15–160 km from the LSA outcrop) and are included in this study for comparison.

High-silica adakite (HSA) samples were collected from a large outcrop ~45 km west of Choir, close to the Tsagandelger area (Fig. 1). These lavas are located on the Middle Gobi volcanic belt (Badarch et al., 2002). In the Tsagandelger area, numerous other Mesozoic volcanic rocks occur within graben structures. As described by Dash et al. (2015), these rocks, here termed Group 2, are shoshonite and absarokite in composition, and in the Tsagandelger area have been dated at 114 ± 0.7 Ma ($^{40}Ar/^{39}Ar$ method).

3. Petrography

The LSA lavas are hypocrystalline with a glomeroporphyritic texture (Fig. 2A). The main glomerocrysts are formed of plagioclase feldspar and augite. There are occasional sanidine phenocrysts as well as rare sericitisation of plagioclase. The groundmass makes up ~80% of the rock volume and is dominated by plagioclase feldspar (some containing apatite inclusions) and minor opaque minerals.

The HSA samples are fresh, glomeroporphyritic, hypocrystalline and contain more glass than the LSA lavas (Fig. 2B). The glomerocrysts are composed of clinopyroxene (augite and minor pigeonite) and there are separate phenocrysts of enstatite (Fig. 2C) and plagioclase feldspar. Some of the enstatite crystals show evidence of resorption and there are also clusters of quartz crystals with melted/resorbed edges (Fig. 2D). The groundmass makes up ~90% of the rock volume and consists primarily of plagioclase feldspar.

Group 1 trachyandesite outcrops have undergone weathering, are vesicular (commonly infilled with siliceous material) and have oxidised and weathered tops. Samples (TCS 2.1, 3.1 & 4.1) contain carbonate amygdales. The trachyandesite lavas are hypocrystalline and the groundmass contains abundant plagioclase, altered clinopyroxene and rare iddingsitised olivine (Fig. 2E–F). Plagioclase crystals have undergone partial (<5%) sericite alteration. Plagioclase phenocrysts sometimes have sieve textures and oscillatory zoning, whereas some of the feldspar crystals, in the groundmass, contain apatite inclusions. Sample TCS 13.1 contains rosetta plagioclase phenocrysts and nepheline phenocrysts. A single trachyte sample, TCS 5.1, is hypocrystalline, contains crustal xenoliths, megacrysts of alkali feldspar and abundant antecrysts of plagioclase, which exhibit sieve textures and resorption features. This trachyte also contains altered clinopyroxene, alkali feldspar phenocrysts and aegirine phenocrysts which have oxidised and magnetite-rich reaction coronas (Fig. 2G–H).

The Group 2 trachyandesite lavas, near the HSA outcrop (~6–155 km), are described as having porphyritic textures with phenocrysts of hypersthene, augite, amphibole, mica and feldspar (Dash et al., 2015). The groundmass is dominantly glass and plagioclase.

4. Argon dating results

Age spectra and inverse isochron ages ($^{36}Ar/^{40}Ar$ versus $^{39}Ar/^{40}Ar$) were calculated for incremental heating experiments (Table 1). The $^{40}Ar/^{39}Ar$ plateau diagrams are presented in Fig. 3. The analytical methods are found in the online supplementary material.

Despite sample TCS 4.1 having a short plateau (38.6% ^{39}Ar), it consists of many steps (n = 15) which suggests the preservation of an age component representative of the crystallisation age. The large staircase of ages in the early steps (Fig. 3A) likely reflects sample alteration (clay formation in plagioclase). Each step heating

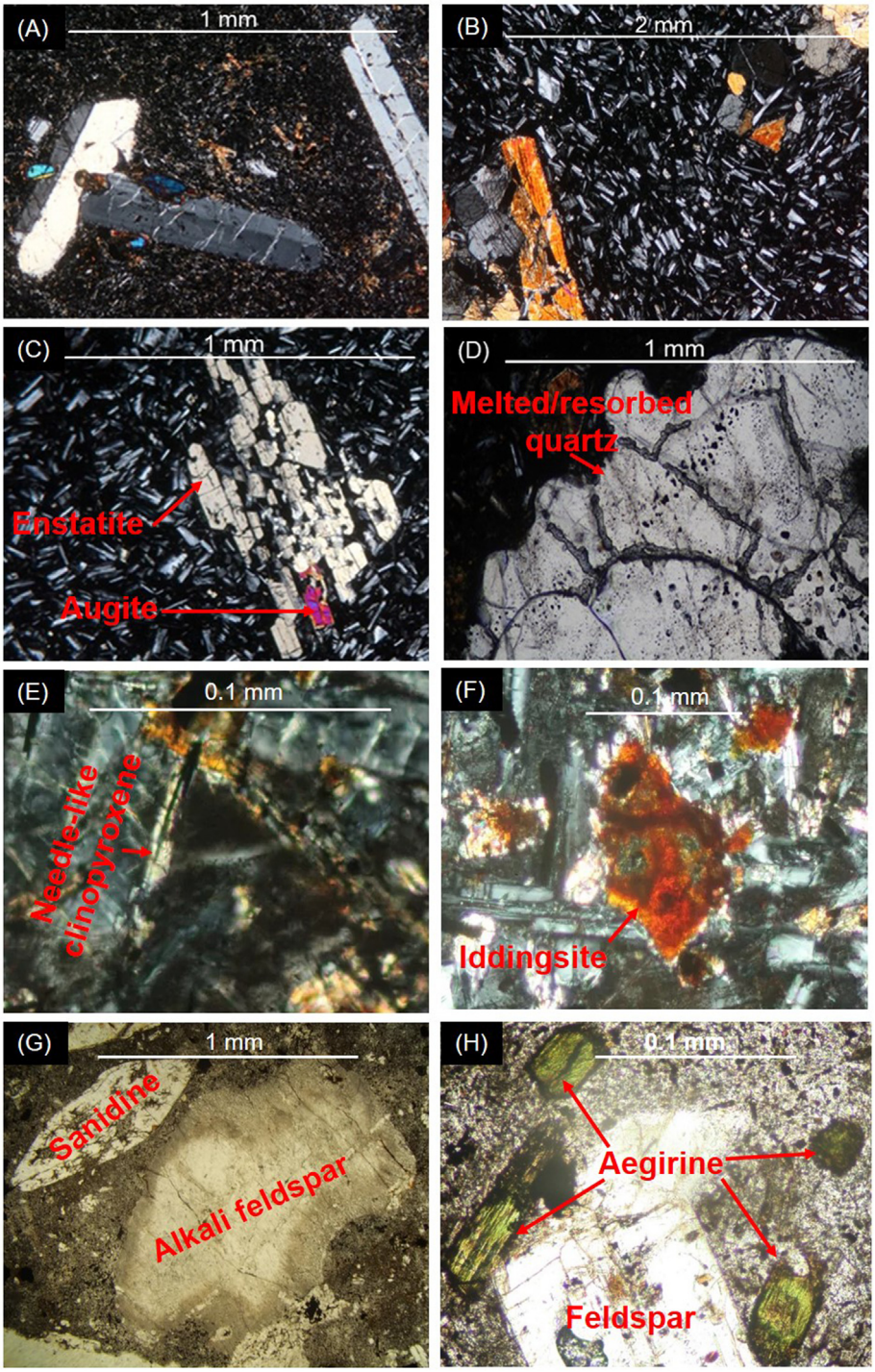

Fig. 2. Photomicrographs of low-Si adakite (A), high-Si adakite (B–D), trachyandesite (E & F) and trachyte (G & H) samples. Photomicrographs A-F in XPL and G-H in PPL: (A) sanidine, plagioclase and augite phenocrysts; (B) glomerophyritic texture; (C) an enstatite and augite phenocryst showing resorption features; (D) melted quartz crystals; (E) needle-like clinopyroxene as groundmass crystals; (F) microphenocrysts of iddingsitised olivine; (G) altered alkali feldspar xenocryst partially enclosed by quartz crystals; and (H) aegirine phenocrysts with magnetite-rich coronas.

Table 1
Summary of Argon dating results.

Sample	$\%^{39}Ar$	Steps in plateau (n)	Plateau age (Ma)±2s	Isochron age (Ma)±2s	Isochron MSWD
TCS 4.1	38.6	15	120.7 ± 0.4	119.0 ± 2.3	1.42
TCS 7.1	58.1	7	138.4 ± 2.8	139.2 ± 6.1	4.7
TCS 7.7	49.4	12	138.8 ± 0.4	138.8 ± 0.4	1.29
TCS 59.2	80.6	24	229.8 ± 0.6	230.3 ± 1.1	1.28

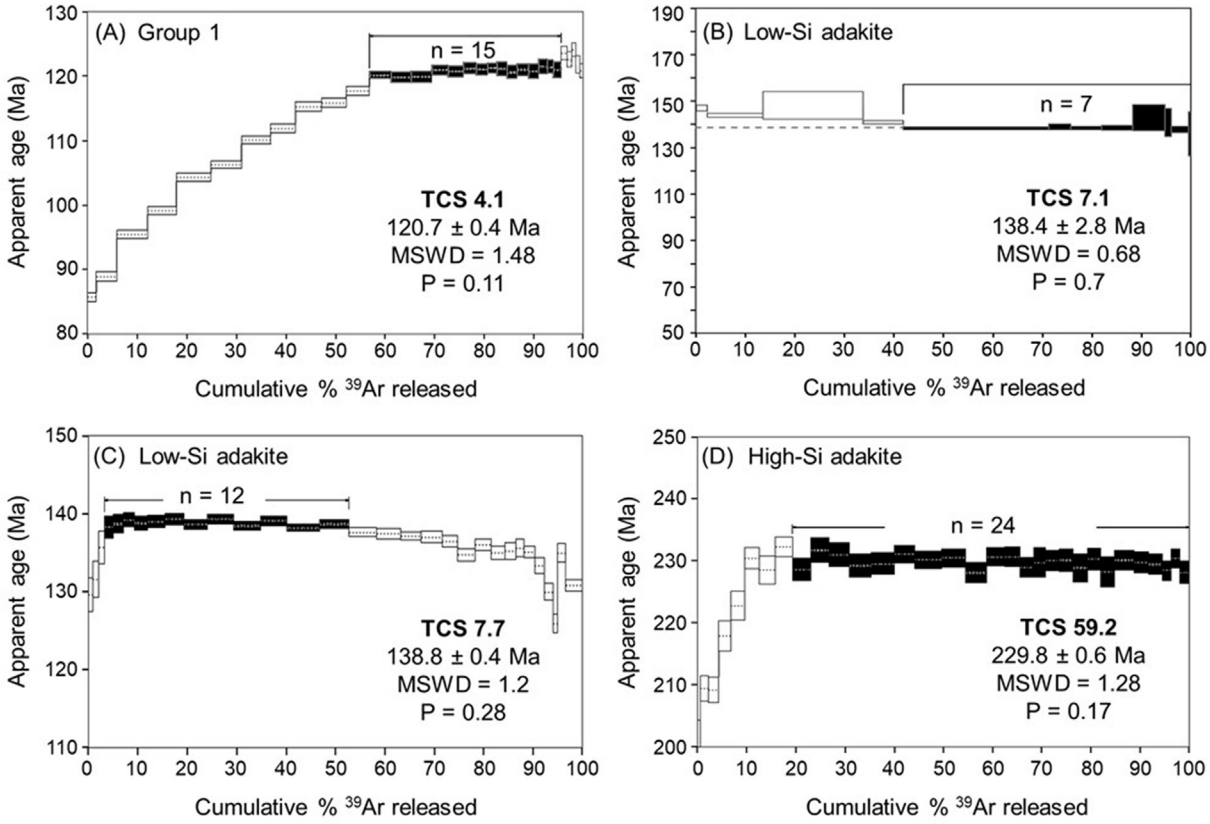

Fig. 3. ^{40}Ar-^{39}Ar age plateau diagrams: (A) Group 1 sample TCS 4.1; (B-C) low-Si adakites (sample TCS 7.1 & TCS 7.7); and (D) high-silica adakite sample TCS 59.2. Also shown on each plateau diagram is the MSWD (mean square weighted deviation) and P (Chi Squared value).

experiment was run at high-resolution, meaning that many steps was utilised, in this case, n > 30. A high-resolution approach was used to attempt to 'see through' or unmix alteration and trapped components from radiogenic argon containing emplacement age information.

The two LSA samples (TCS 7.1 and 7.7) have plateau ages of 138.4 ± 2.8 and 138.8 ± 0.4 Ma respectively, which is in good agreement with calculated isochron ages of 139.2 ± 6.1 and 138.8 ± 0.4 Ma. The HSA sample (TCS 59.2) has a plateau age of 229.8 ± 0.6 Ma and is in good agreement with the isochron age of 230.3 ± 1.1 Ma. Finally, the Group 1 sample (TCS 4.1) has a plateau age of 120.7 ± 0.4 Ma and an isochron age of 119.0 ± 2.3 Ma.

Herein, we take the plateau age to represent the crystallisation age of our dated samples (Fig. 3).

5. Geochemical results

5.1. Rock classification and major-element variations

The analytical methods and data are found in the online supplementary material. The LSA, HSA and Group 1 samples have loss-on-ignition (LOI) values < 2 wt %, other than sample TCS 7.5, which has a LOI value of 4.75 wt %. Only one sample (4/2) from Group 2 has a LOI value > 3. wt. %. Due to the higher LOI value for sample TCS 7.5 this sample is omitted from further study.

Rock classifications are presented in Fig. 4 using a SiO_2 wt. % vs. Nb/Y immobile element plot from Winchester and Floyd (1977). The LSA samples plot in the trachyandesite field, while the HSA samples plot in the dacite field. Group 1 and 2 samples plot predominantly in the basaltic-trachyandesite/trachybasalt to trachyandesite field. Sample TCS 5.1, from Group 1, classifies as a trachyte. The SiO_2 versus $Na_2O + K_2O$ classification system (after Irvine and Baragar, 1971) discriminated the LSA samples as belonging to the alkaline series and the HSA samples in the sub-alkaline series (Fig. 5A). Other than three samples (TCS 5.1, TCS 13.1 and 4/626), the Group 1 and 2 samples plot in the alkaline series. The LSA and Group 1 samples have K-contents consistent with shoshonitic rocks or high-K rocks (Fig. 5A). The discriminant scheme from Hastie et al. (2007) uses elements Th and Co to further classify sub-alkaline volcanic rocks. On this Th-Co classification diagram, the HSA samples plot in the high-K/shoshonite field (Fig. 5B).

On a Y vs. Sr/Y plot (Fig. 6A), the LSA samples form a trend between end-member compositions for typical trachyandesite/trachyte and an adakite array. The HSA samples plot fully within the adakite array. Other than two samples (3/11 & 3/12) from Group 2, the Group 1 and 2 samples plot within the typical trachyandesite/trachyte array.

5.2. Trace-element and REE variations

The LSA and HSA samples have increasing La/Yb ratios with decreasing Yb (Fig. 6B) and the Group 2 samples have decreasing Zr concentrations with increasing SiO_2 (Fig. 7A). The LSA, Group 1 and 2 samples have clear correlations between SiO_2 and P, Sm and Yb (Fig. 7 B–G).

On the primitive mantle-normalised and chondrite normalisation diagrams (Fig. 8) the LSA, HSA, Group 1 and 2 samples are all enriched in the light rare-earth elements (LREE), high-field strength elements (HFSE) and large-ion lithophile elements (LILE) compared to *N*-MORB (normal mid-ocean ridge basalt; Gale et al., 2013). Furthermore, the study samples are much more depleted

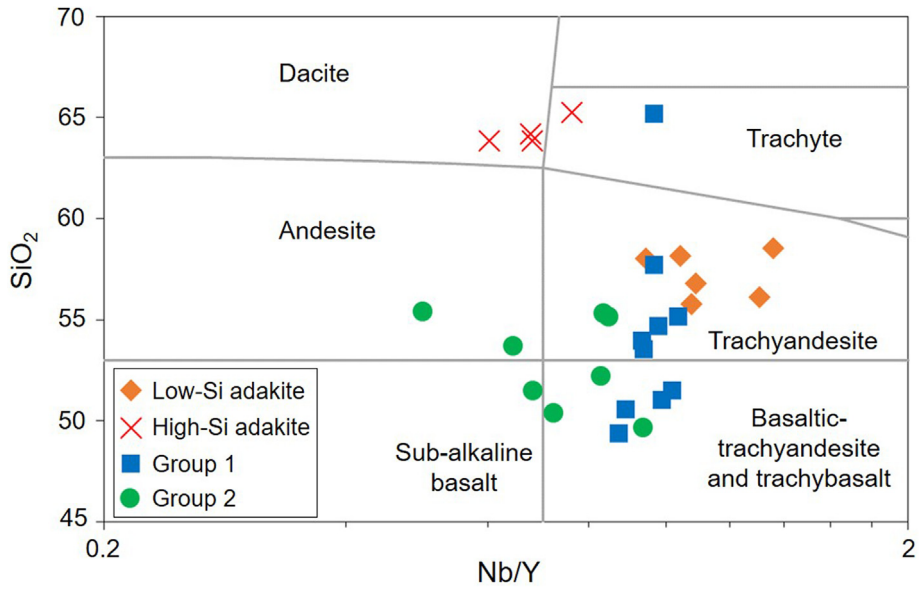

Fig. 4. Nb/Y vs. SiO_2 wt. % immobile element rock classification diagram (from Winchester and Floyd, 1977) for all analysed samples.

in the heavy rare-earth elements (HREE) compared to *N*-MORB, and have negative Nb and Ta anomalies. All the LSA samples have negative Y anomalies (Fig. 8A). In addition to all the samples having positive Pb anomalies they also have negative Sm and Ti anomalies. The LSA samples have positive Ba anomalies and are more enriched in the LREE and MREE compared to the HSA samples (Fig. 8A). The HSA samples are more enriched in Rb, Th and U but have much lower concentrations of Nb and Ta compared to the LSA samples. Group 1 and 2 samples commonly have positive Ba anomalies (Fig. 8B). All the samples are enriched in the fluid-mobile incompatible elements (e.g., Rb, Ba, K) compared to ocean island basalt (OIB; Sun and McDonough, 1989) and average continental arc basalt (CAB; Kelemen et al., 2003). Similarities between CAB and the Mongolian samples are evident from the mirroring of many element anomalies. However, all the Mongolian samples are more enriched in LILE, HFSE and LREE than CAB. The LSA and HSA samples, plus some of the Group 2 samples, are more depleted in HREE than typical CAB.

6. Fractional crystallisation

No olivine phenocrysts were identified in the LSA and HSA samples; this suggests that if there was any olivine fractionation, then it must have occurred in the parental magma. However, olivine fractionation is evident in Group 1 samples because iddingsitised olivine phenocrysts were identified in thin section studies (Fig. 2).

Petrological studies identified augite in the LSA, HSA and Group 1 samples, as well as in Group 2 lavas by Dash et al. (2015), suggesting it was a fractionating phase. Decreasing Dy/Dy* vs. Dy/Yb (Fig. 7H) trends in all sample suites further indicate clinopyroxene fractionation.

Chondrite-normalised Eu/Eu* numbers $[\frac{Eu}{Eu^*} = (\frac{Eu_n}{((Sm_n+Gd_n)0.5)})]$ range from 0.87 to 0.95 for the LSA samples and 0.83 to 0.95 for the HSA samples; this does not indicate significant plagioclase fractionation (or accumulation). Group 1 and 2 samples have Eu/Eu* numbers ranging from 0.74 to 0.84 and 0.66 to 0.86 respectively, and correlates positively with Sr, suggesting plagioclase fractionation was more significant than in the LSA and HSA (Fig. 7I).

Zircon and apatite fractionation can deplete melts of HREEs. The Group 2 samples and possibly the LSA samples have negative correlations between Zr and SiO_2 likely reflecting zircon fractionation (Fig. 7A). The primitive mantle-normalisation diagrams show samples from all suites have negative Sm anomalies, possibly because of apatite fractionation (Fig. 8A–B). Furthermore, other than the HSA samples, clear trends are seen between P and SiO_2, and Yb and Sm supporting apatite fractionation (Fig. 7B–G). The negative Y anomalies, along with low abundances of the HREEs (e.g., Yb, Lu) on the primitive mantle plots (Fig. 8A–B), for the LSA and HSA samples likely reflect residual garnet.

7. Source characterisation

On a plot of SiO_2 versus Mg-number (Fig. 9) the LSA samples plot within the "slab melts" field (Sen and Dunn, 1994; Rapp et al., 1999, and references therein) and typically have lower Mg-numbers (from 0.33 to 0.39, where Mg-number = {molar Mg/(Mg + Fe^t)}) than the HSA samples (0.31–0.49) which are more enriched in $Fe_2O_{3(T)}$. If the LSA and HSA were derived from the same source, then this lower Mg-number for the LSA would not be consistent with a simple model that invoked assimilation of more mantle peridotite, as we would expect the LSA to have higher Mg-numbers. However, the LSA samples have Mg-numbers comparable to Group 1 lavas, between 0.21 and 0.39.

The HSA samples also lie in, or close, to the "slab melting" field for SiO_2 versus Mg-number, next to results for "slab" + peridotite melting experiments (Rapp et al., 1999), suggesting only minor mantle assimilation, or extensive fractional crystallisation processes. Most of the HSA samples are comparable to global examples of Cenozoic adakites (Fig. 9) and have similar Mg-numbers to Carboniferous Mongolian adakites from the Shuteen Complex (Batkhishig et al., 2010). Three of the HSA samples have Mg-numbers ranging from 0.47 to 0.49 at >63 wt % SiO_2. However, although the HSA samples have higher Mg-numbers than some adakitic crustal melts (Fig. 9; Lingqiu Basin and Huichang Basin), they are comparable to others (Fig. 9; Ningzhen area, east China; and Awulale-Sanchakou (A&S), of the Xinjiang Tianshan region, China) which have been hypothesised to have interacted with mantle material (Xu et al., 2002; Zhao et al., 2008).

To further consider source characteristics, we can compare our data to melting experiments that produced adakitic melts (e.g., Rapp et al., 1991, 1999; Sen and Dunn, 1994; Wolf and Wyllie, 1994;

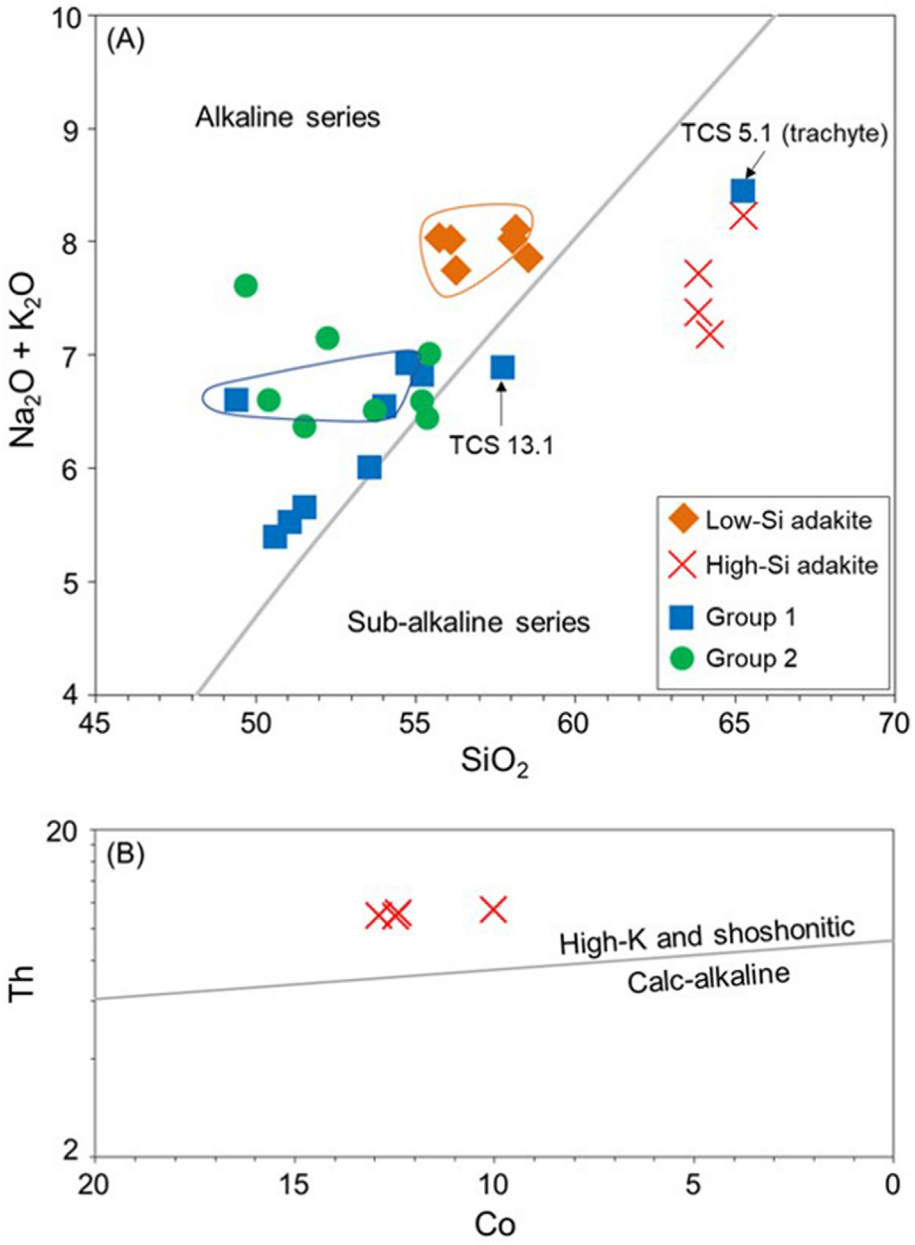

Fig. 5. (A) SiO_2 wt. % vs. $Na_2O + K_2O$ wt. % plot (from Irvine and Baragar, 1971) for all analysed samples. Shoshonitic low-Si adakite and Group 1 samples are highlighted based on the classification scheme from Ewart (1983). (B) A plot from Hastie et al. (2007) of Co vs. Th (ppm), for the HSA samples.

Rapp and Watson, 1995). Using these studies, geochemical fields were generated for adakitic liquids produced from partial melts of basaltic compositions (Fig. 10). Geochemical fields were classified in the work by Xiong et al. (2003) and are summarised in Table 2.

Also included on these plots (Fig. 10 A-F) is the adakite field from Xiong et al. (2003, and references therein). This adakite field was generated from 11 Cenozoic global adakite localities: Aleutian Arc, Alaska; Cook Island, Chile; Baja of California, Mexico; Sierra Madre, Mexico; Skagway, Alaska; Mindanao, Philippines; Southwest Japan; Austral Andes and Quimsacocha, Ecuador.

The LSA samples have major-element characteristics where some (or all) of the samples plot outside the adakite field (Fig. 10) or any of the melt experiment fields (Fig. 10 A, B, C, E & F). They have less Al_2O_3, less CaO and more K_2O than the melts produced from the low-K, -Na and high-Na, -Mg amphibolite (WW) and thus it seems unlikely that this would be an appropriate protolith. Furthermore, the LSA samples have less Al_2O_3, Na_2O and more CaO than the experimental partial melts of alkali-rich basalt (R_1). Other than for Na_2O, the LSA samples also plot outside the $R_{2\text{-}4}SW$ field (e.g., for Al_2O_3, FeO and K_2O; Fig. 10 A, C & F). On the plots where the LSA samples plot within the $R_{2\text{-}4}SW$ field (Fig. 10 B & E) it appears to be a trend into this field; such a trend could reflect late-stage fractionation processes.

The HSA samples have significantly less Al_2O_3 (Fig. 10A) and CaO (Fig. 10E), and are more enriched in Na_2O and K_2O (Fig. 10 D & F), than the 10 kbar amphibolite partial melts (WW) and thus arguably preclude a similar protolith composition. Furthermore, the HSA samples have less Al_2O_3 (Fig. 10A), Na_2O (Fig. 10D) and more CaO (Fig. 10E) than the alkali-rich basalt partial melts (R_1; these experiments were also done at a range of pressures between 12 and 38 kbar) suggesting this also may be an unsuitable protolith. Most HSA samples plot in the $R_{2\text{-}4}SW$ field. However, some HSA samples

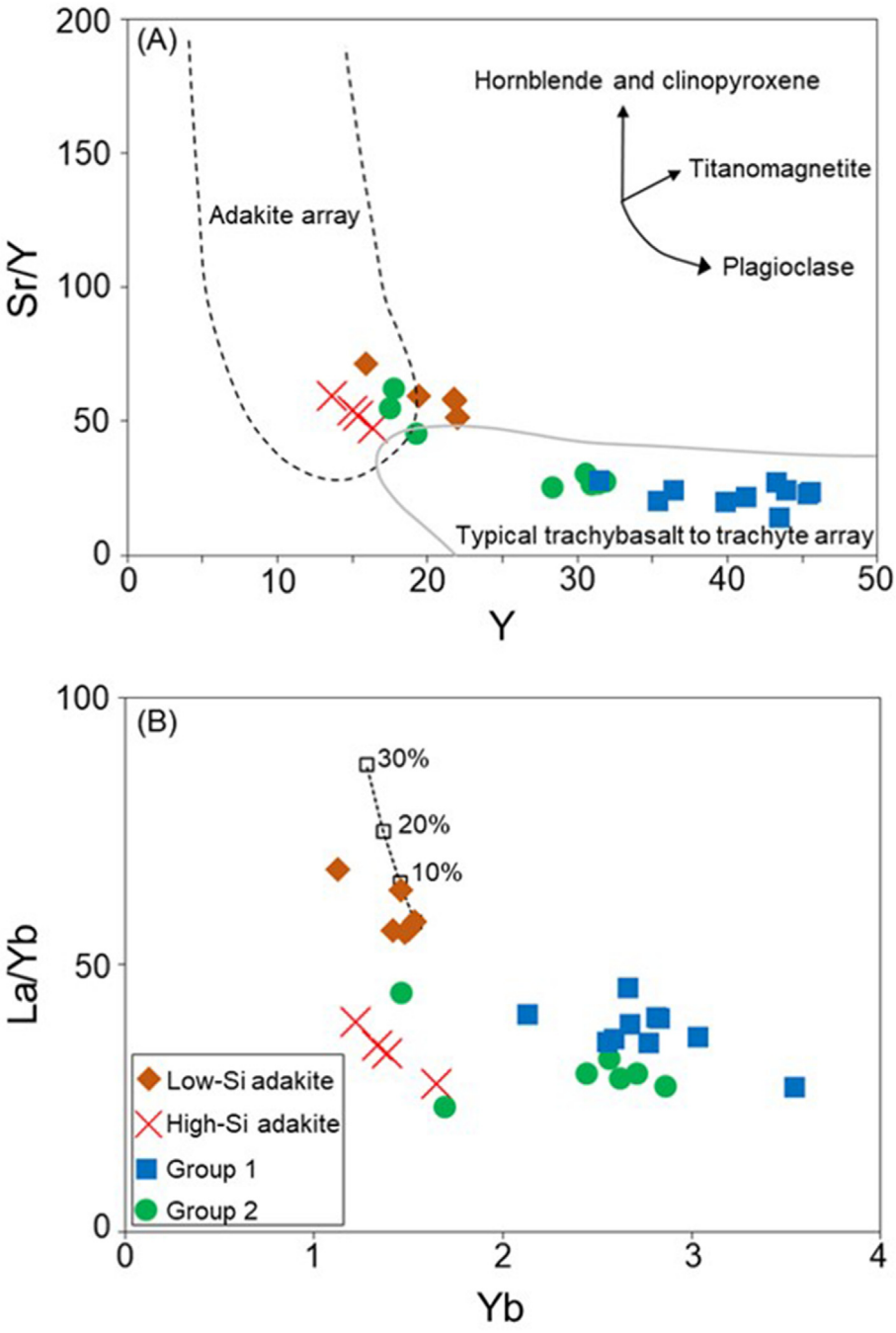

Fig. 6. (A) Y (ppm) vs. Sr/Y (after Hansen et al., 2002) and (B) Yb (ppm) vs. La/Yb plots. A calculated Rayleigh fractional crystallisation curve (20% clinopyroxene, 77% plagioclase, 2% zircon and 1% apatite) is shown on Figure B. The partition coefficients utilised are calculated from alkali basalt and trachyandesite compositions (Fujimaki, 1986; Luhr et al., 1984) and the amount of fractionation is shown next to the curve (a maximum of 30% is shown).

don't plot in the $R_{2\text{-}4}SW$ field for Al_2O_3 (Fig. 10A) and only one of the samples plots in this field for MgO (Fig. 10B). Other than for Al_2O_3 and K_2O (Fig. 10 A & F), the HSA samples commonly plot in the adakite field. Although enrichment in K_2O has been used to suggest that Mesozoic adakites from China are crustal melts (e.g., Wang et al., 2006), this criterion alone is insufficient. For example, most of the Carboniferous Shuteen Complex adakites are more enriched in K_2O than other global adakite examples, and depleted in Al_2O_3 (Fig. 10 A & F), yet have $^{87}Sr/^{86}Sr_i < 0.704$ which argues against a crustal melt origin. However, the HSA samples are most similar in affinities to high-pressure melting experiments that suggest a *N*-MORB-source.

If we consider trace-element abundances, melting of eclogite should produce melts with lower Cr and Ni concentrations than melts from mantle peridotite (e.g., Castillo, 2006). Therefore, melts of an eclogite lower crust, which has undergone minor, or no mantle interaction, will also have lower Cr and Ni concentrations than mantle peridotite melts. However, because any slab melt must pass through any overlying mantle, these melts should become enriched in Cr and Ni during mantle assimilation processes.

The LSA samples have Cr and Ni concentrations higher than the crustal melts which have undergone minor or no mantle assimilation (Fig. 11; Lingqiu Basin, North China Craton; Ningzhen area, east China; Huichang Basin, China). The Cr and Ni concentrations

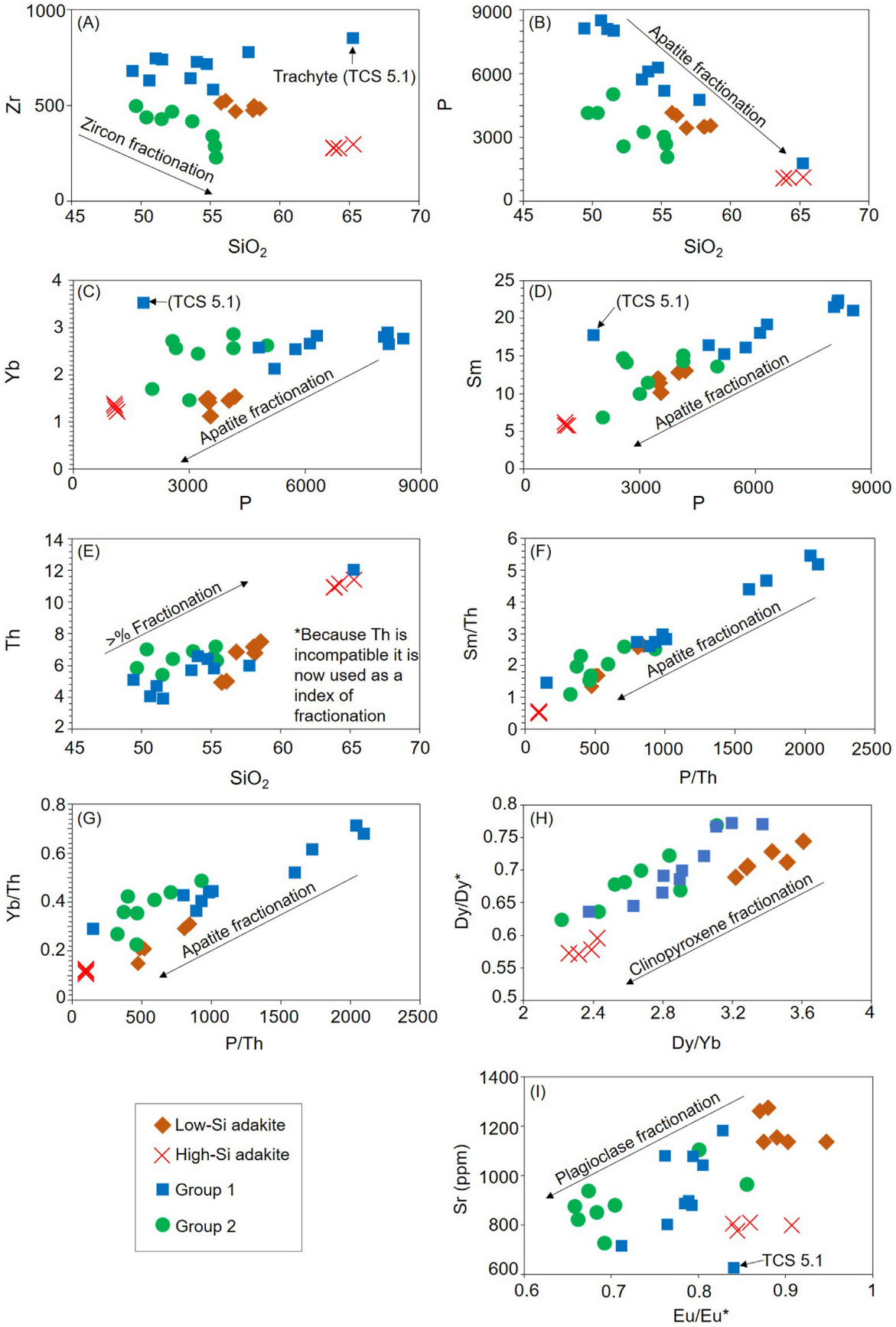

Fig. 7. Variations in major-element oxides (wt. %) and trace elements (ppm) for the low-Si adakites, high-Si adakites, Group 1 and 2 samples. Where $\frac{Dy}{Dy^*} = \frac{Dy_n}{La_n^{4/13} Yb_n^{9/13}}$ (Davidson et al., 2012). The chondrite normalisation values are from Sun and McDonough (1989).

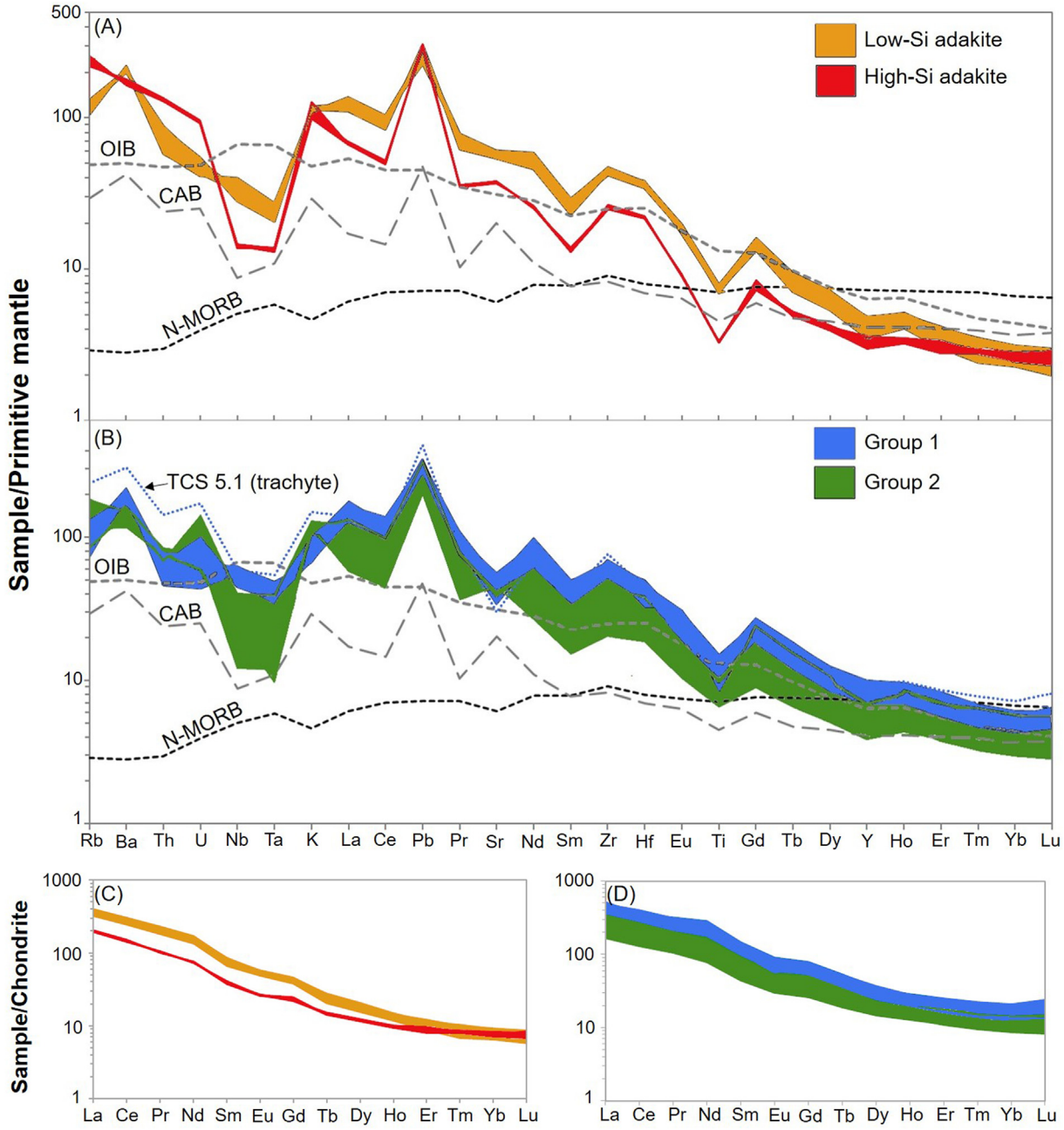

Fig. 8. (A–B) Primitive mantle-normalised trace-element variation diagrams; (C–D) Chondrite normalisation diagrams (Sun and McDonough, 1989). Data sources: OIB: Sun and McDonough (1989); average CAB: Kelemen et al. (2003) and *N*-MORB: Gale et al. (2013).

are also higher than in the Group 1 lavas, and a negative correlation with SiO_2 suggests a fractionation control.

The HSA samples also have Cr and Ni concentrations higher than many crustal melts which have undergone minor or no mantle assimilation (Fig. 11) but plot along with Cenozoic adakites or with hypothesised crust + mantle melts (e.g., Ningzhen area). Lower crustal foundering has been hypothesised as one method to explain how a mafic lower crust could interact with mantle material (e.g., Gao et al., 2004). Thus, the HSA samples have Ni and Cr concentrations most likely reflecting slab + mantle melts, or crust + mantle melts.

In global studies, adakitic melts have also been identified by considering Nb/Ta ratios (e.g., Condie, 2005). This is because continental crust has low average Nb/Ta ratios (10.9–13; Rudnick and Fountain, 1995; Rudnick and Gao, 2003), compared to MORB (16.7 ± 1.8; Kamber and Collerson, 2000) or primitive mantle (17.5 ± 2; McDonough and Sun, 1995). However, rutile partitions Nb and Ta, but fractionates them from one another (Foley et al., 2000; Liang et al., 2009; Xiong et al., 2011; Gan et al., 2019). Therefore, melts in equilibrium with residual rutile should be characterised by high Nb/Ta ratios (e.g., Gao et al., 2004; Xiong et al., 2005). A mantle that has been metasomatised by small degree partial melts of an eclogite may also have high Nb/Ta ratios (e.g., Foley et al., 2002). In summary, initial melts of rutile-bearing eclogite should have relatively high Nb/Ta ratios. However, progressive melting of this eclogite would exhaust rutile, therefore resulting in melts with low Nb/Ta ratios inherited from earlier melt depletion (e.g., Liu et al., 2008). Based partly on low Nb/Ta ratios, Condie (2005) determined that adakitic tonalite-trondhjemite-granodiorites may be produced from partial melting of hydrous mafic rocks in the lower

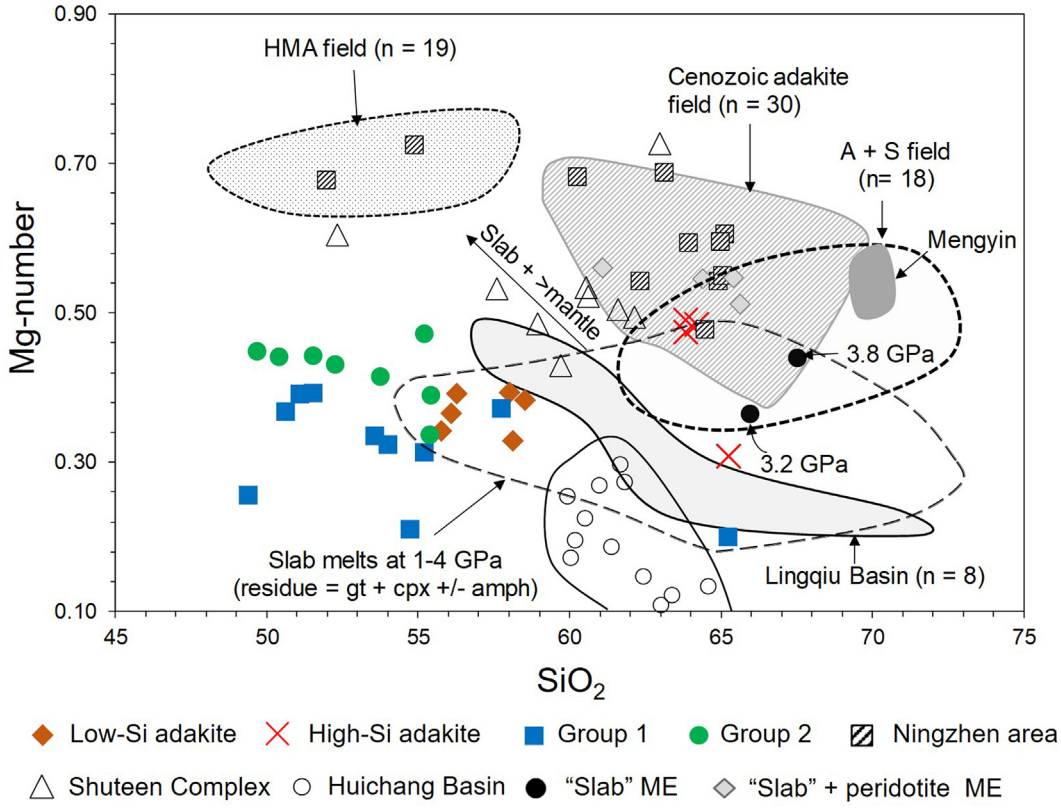

Fig. 9. SiO_2 wt. % vs. Mg-number (where Mg-number = {molar Mg/(Mg + Fe^t)}) plot. The "high-Mg andesite field" (HMA) represent oceanic eclogitic melts that interacted with the mantle wedge (Xu et al., 2000; Bryant et al., 2011). Shuteen Complex (Mongolia) adakites from Batkhishig et al. (2010) and Mengyin adakites (east China) from Wang et al. (2016). Ningzhen area (east China) samples were interpreted as delaminated lower crust which assimilated mantle (Xu et al., 2002). Huichang Basin, SE China (Xiong et al., 2003), and Lingqiu Basin, North China (Wang et al., 2006) samples represent melts of an underplated basaltic lower crust. The "A + S" field represent Awulale and Sanchakou (Xinjiang Tianshan region, China) adakitic rocks and are interpreted as a product of basaltic underplating at the base of the lower crust (Zhao et al., 2008). The "slab" melting and "slab" + peridotite (mantle) melting experiments (ME) and the 1–4 GPa "slab melts" field is based on data from Rapp et al. (1999, and references therein). The Cenozoic adakite field was generated from data within Aguillón-Robles et al. (2001) and Stern and Kilian (1996); Vizcaino Peninsula, Mexico; Lautaro; Viedma, Aguilera, Reclus; Mt Burney and Cook Island.

crust (with Nb/Ta ratios averaging ~5) and are thus unlike slab melts. As discussed by Condie (2005), most Nb data from XRF must be rejected and only high precision ICP-MS Nb and Ta should be used; hence the data is plotted on the same diagram as Condie (2005) using ICP-MS data for these elements (Fig. 12).

The LSA and HSA samples have an average Nb/Ta ratio of 24.6 (±0.77) and 18.38 (±0.85) respectively. Therefore, the LSA samples have high Nb/Ta ratios consistent with a source that contained residual rutile or underwent metasomatic processes (e.g., by melts from a rutile-bearing protolith). The HSA samples have lower Nb/Ta ratios which are close to average MORB and primitive mantle, consistent with the experimental melt comparisons (Fig. 10). Thus, the HSA samples have Nb/Ta ratios consistent with rutile-eclogite melting, albeit, they plot out of the adakite field defined in Condie (2005). The Group 1 samples (excluding the single trachyte sample – TCS 5.1) have an average Nb/Ta ratio of 22.78 (±0.79), whereas the Group 2 samples have an average Nb/Ta ratio of 18.4 (±0.84). Therefore, the Group 1 and 2 samples have Nb/Ta ratios higher than average continental crust and likely reflect melting from a source which underwent metasomatism possesses. The lower Nb/Ta ratios in the Group 2 samples might reflect melting from a less metasomatised source, and/or increased crustal involvement.

8. Isotope variations and crustal input

Initial $^{87}Sr/^{86}Sr_{(i)}$-$\varepsilon Nd_{(t)}$-$Pb_{(i)}$-$\varepsilon Hf_{(t)}$ values are calculated for the HSA (230 Ma), LSA (138 Ma) and Group 1 (121 Ma) samples (Figs. 13 and 14). The low MgO and fractionation of late-stage minerals indicates that none of these melts are primary and thus likely had opportunity for crustal contamination. The crustal cumulates in the HSA samples also indicate crustal assimilation processes.

All the LSA, HSA and Group 1 samples have $^{87}Sr/^{86}Sr_{(i)}$ vs. $\varepsilon Nd_{(t)}$ values that plot in the mantle array (Fig. 13A). The similar $^{87}Sr/^{86}Sr_{(i)}$ and $\varepsilon Nd_{(t)}$ values for the LSA and Group 1 samples might reflect comparable source compositions. The HSA have positive $\varepsilon Nd_{(t)}$ values (0.48–1.17) unlike most of the crustal adakitic rocks from China. Furthermore, the HSA have $^{87}Sr/^{86}Sr_{(i)}$ values (0.7051–0.7053) close to some Cenozoic adakites, with values lower than most crustal derived adakitic rocks from China (Fig. 13A); however, the HSA also have $^{87}Sr/^{86}Sr_{(i)}$ vs. $\varepsilon Nd_{(t)}$ values like the Awulale adakitic rocks which are interpreted as a product of basaltic underplating of amphibole-eclogite facies (Zhao et al., 2008). To test whether assimilation-fractional crystallisation (AFC) could change a typical adakite signature ($^{87}Sr/^{86}Sr$ = ~0.704 and high εNd values) to values close to the HSA, AFC (DePaolo, 1981) modelling was done. Because Carboniferous adakites from the Shuteen Complex (South Mongolia) are interpreted as slab melts (Batkhishig et al., 2010) a sample (SH-18) from this group is used as a starting composition. The crustal contaminant was a granulite crustal xenolith from southern Mongolia (Barry et al., 2003) and a value (assimilation/crystallisation rate) of r = 0.5 is used. The AFC modelling indicates that the HSA could be from a parental magma with similar $^{87}Sr/^{86}Sr_{(i)}$ and $\varepsilon Nd_{(t)}$ compositions to the Shuteen

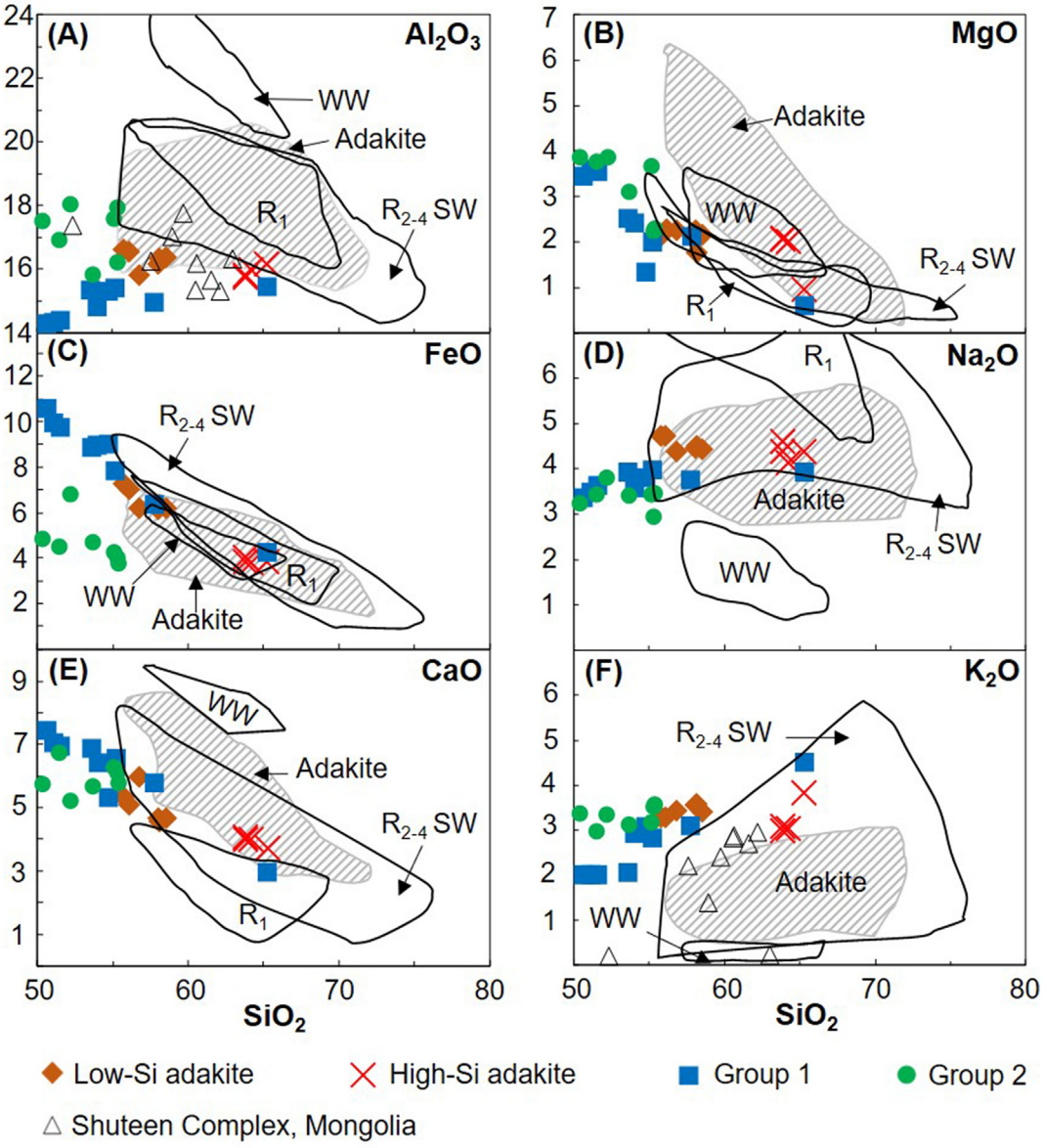

Fig. 10. Oxide wt. % compositional comparison of the different sample suites with adakites and high pressure (≥10 kbar) partial melts of basalt (Xiong et al., 2003, and references therein). Also included are the Carboniferous adakites from the Shuteen Complex, Mongolia (Batkhishig et al., 2010). The different fields correspond to: R_1 = partial melts of alkali basalt at 12–38 kbar; $R_{2\text{-}4}$SW = partial melts of basalts compositionally close to *N*-MORB at 10–32 kbar; WW = partial melts of a low-K, low-Na, high-Mg, high-Ca basalt at 10 kbar. This adakite field was generated from 11 Cenozoic adakite localities: Aleutian Arc, Alaska; Cook Island, Chile; Baja of California, Mexico; Sierra Madre, Mexico; Skagway, Alaska; Mindanao, Philippines; Southwest Japan; Austral Andes and Quimsacocha, Ecuador. Symbols are the same as in Fig. 9.

Complex adakites but with additional crustal input (Fig. 13A).

The $\varepsilon Hf_{(t)}$ values for the LSA, HSA and Group 1 samples are similar (2.94–5.59). Despite these values being lower than *P*-MORB (Fig. 13B) they are like values obtained from zircons in the Mengyin adakites (Wang et al., 2016).

The Pb isotopes (Fig. 14) for the LSA, HSA and Group 1 samples have similarly high values. These samples plot above the NHRL, *P*-MORB field and the Awulale adakitic samples but are more comparable to the global Cenozoic and Chinese Mengyin adakites. Group 1 samples have similar Pb isotopic abundances to the LSA

Table 2
Summary of different geochemical groupings.

Group name	No. of sample experiments	Pressure	Starting material	References
R1	13	12 −38 kbar	Alkali-rich basalt with high total alkalis (Na2O + K2O) and low CaO, FeO, MgO and TiO2.	Rapp et al. (1991), (1999); Rapp and Watson (1995); Rapp and Watson (1995).
R2-4SW	59	16 −32 kbar	Compositions close to *N*-MORB. However, some of the starting compositions have slightly higher Na2O and K2O than average *N*-MORB (Hofmann, 1988).	Rapp and Watson (1995), Sen and Dunn (1994) and Winther (1996).
WW	14	10 kbar	low-K and low-Na, high-Mg and high-Ca amphibolite	Wolf and Wyllie (1994)

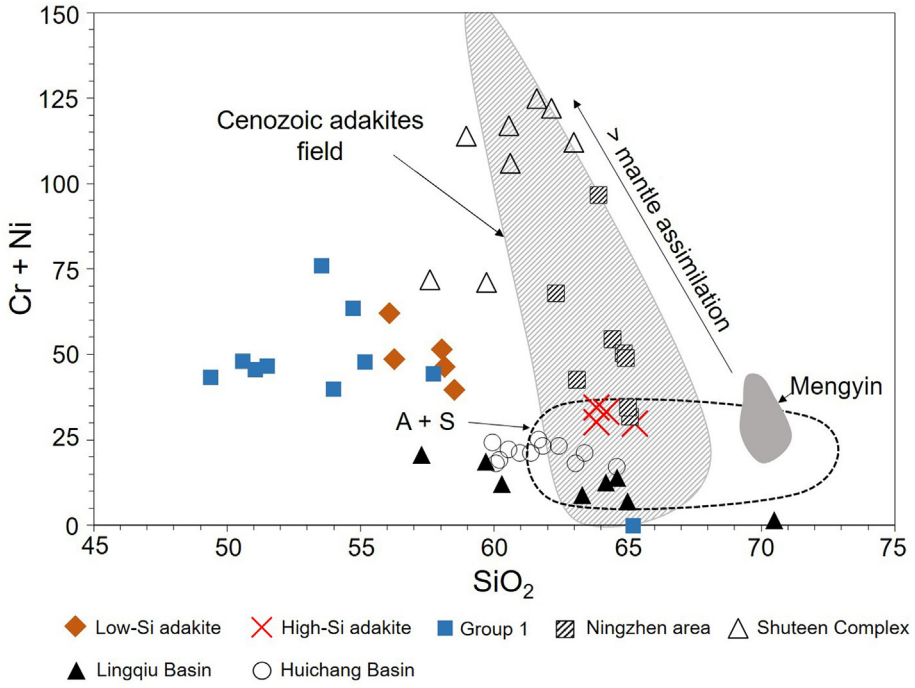

Fig. 11. SiO_2 wt. % vs. Cr + Ni (ppm) plot. Symbols and data sources are the same as in Fig. 9.

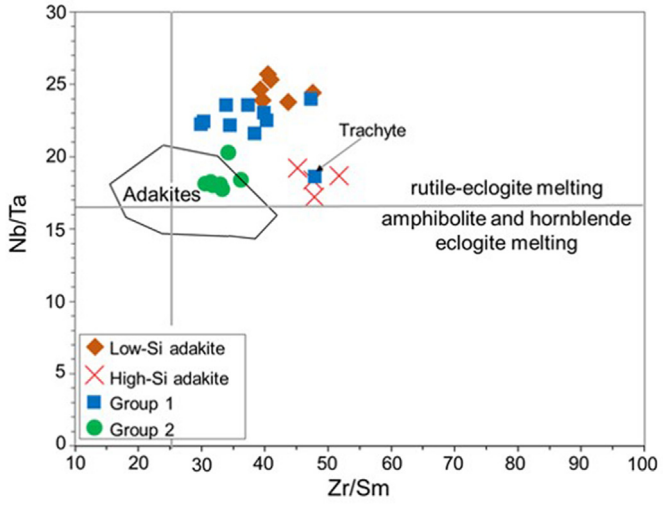

Fig. 12. Zr/Sm vs. Nb/Ta plot. The vertical line represents the average Zr/Sm value for primitive mantle (25.2; Sun and McDonough, 1989) and melting fields from Foley et al. (2002). The adakite field is from Condie (2005). Sample 4/626 from Group 2 is omitted (Nb/Ta = 40).

and HSA despite not having adakite-like major- and trace-element abundances.

9. Discussion

During the Mesozoic, eastern Asia was affected by Paleo-Pacific plate subduction, the closure of the Paleo-Asian Ocean (evident today from the Solonker suture) and the closure of the Mongol-Okhotsk Ocean (e.g., Chen et al., 2009; Windley et al., 2010; Xiao et al., 2015; Torsvik and Cocks, 2016). However, subduction of the Paleo-Pacific plate occurred >2000 km away from Mongolian Mesozoic lava fields (e.g., Van Hinsbergen et al., 2015; Torsvik and Cocks, 2016; Sheldrick et al., 2018) while the closure of the Paleo-Asian Ocean (e.g., Sengör and Natal'in, 1996; Windley et al., 2010) is estimated to be around 296–234 ± 6 Ma (Chen et al., 2009) and therefore may predate all of our samples.

Although the HSA magmatism (230 Ma) possibly coincided with the final closure of the Paleo-Asian Ocean (Chen et al., 2009) the samples are presently ~500 km away from the Solonker suture. However, the HSA magmatism corresponds with the fastest (250-200 Ma) stage of closure of the Mongol-Okhotsk Ocean (Wu et al., 2017) and is presently ~100 km south of the Mongol-Okhotsk suture (Fig. 1). These samples typically have higher $^{87}Sr/^{86}Sr_{(i)}$ and lower $\varepsilon Nd_{(t)}$ values than adakites (Fig. 13A) but the adakitic rocks from China have similarly much higher $^{87}Sr/^{86}Sr_{(i)}$ and lower $\varepsilon Nd_{(t)}$ values. AFC modelling indicates that crustal contamination could modify a typical adakite isotopic signature (i.e. values akin to *N*-MORB) to values close to the HSA samples (Fig. 13A) and the presence of melted quartz cumulates is consistent with assimilation processes. However, the HSA samples also have isotopic values like adakitic rocks which were derived from basaltic underplating (e.g., Zhao et al., 2008). Therefore, it is difficult to favour a model of slab melting or basaltic underplating, for the HSA genesis, from isotope data alone.

The HSA samples have Mg-numbers and MgO wt. % concentrations consistent with mantle assimilation (Figs. 9 & 10B). Furthermore, the relatively low Na_2O and relatively high Ni + Cr concentrations compared to crustal melts also supports mantle assimilation (Figs. 10D & 11). Two models are proposed to explain the petrogenesis of these samples:

(1) A southward-subducting Mongol-Okhotsk slab underwent partial melting during the closure of the Mongol-Okhotsk Ocean. These slab melts then assimilated mantle and finally crustal rocks.
(2) The closure of the Mongol-Okhotsk Ocean thickened the crust. Basaltic underplating of a thickened (>50 km; >1.5 GPa), eclogite lower crust then foundered into the underlying mantle, assimilated minor mantle material and finally underwent crustal contamination.

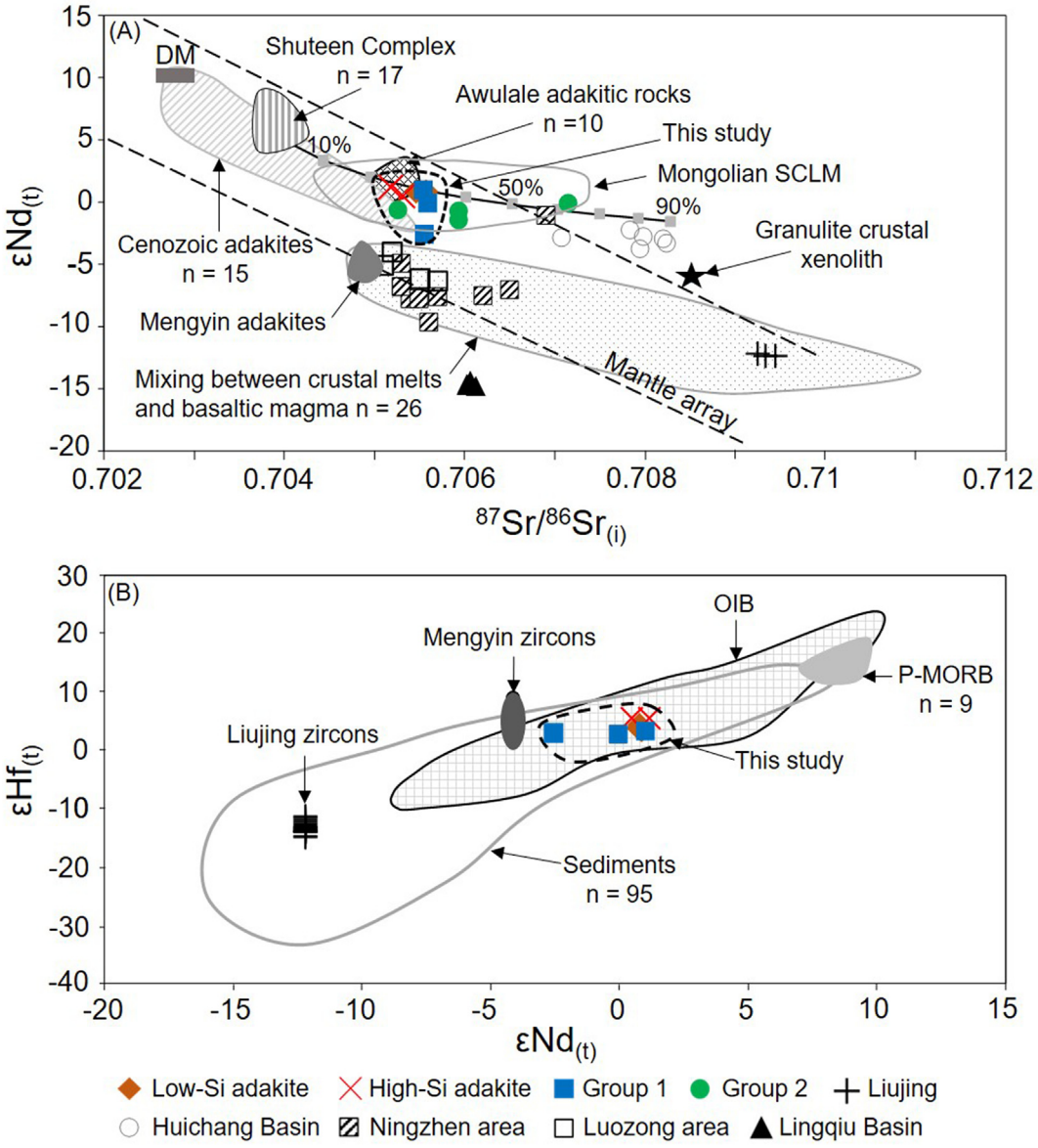

Fig. 13. (A) Plot of $^{87}Sr/^{86}Sr_{(i)}$ vs. $\varepsilon Nd_{(t)}$ and (B) a plot of $\varepsilon Nd_{(t)}$ vs. $\varepsilon Hf_{(t)}$. The mixing of crustal and basaltic melts field is from Chen et al. (2013). The Cenozoic adakites field is generated from: the Andean-Austral volcanic zone (Stern and Kilian, 1996; Lautaro, Viedma, Reclus and Mt. Burney); Cerro Pampa, South America (Kay et al., 1993); La Yeguada Volcanic Complex, Panama (Defant et al., 1991) and Vizcaino Peninsula, Mexico (Aguillón-Robles et al., 2001.). The *P*-MORB field generated from: Alexander Island, Antarctica; SW & NW Pacific crust and Venezuela (Barry et al., 2017 and references therein). Mongolian lithospheric melts field based on data from Sheldrick et al. (2018, and references therein). The depleted mantle (DM) is from Zindler and Hart (1986); mantle array is from Zhang et al. (2005); OIB field from Wang et al. (2016; and references therein) and sediment field from Vervoort et al. (1999) but excluded the Archean shales. The AFC modelling (equations from DePaolo, 1981) utilises a r value 0.5 and the starting composition used sample SH-18. The amount of F ranges from 1 to 0.1 and tick marks are in 10% intervals. The granulite contaminant (TB95–2.5) is from Barry et al. (2003) and isotopic values are age adjusted to 230 Ma. Other data from the same cited sources utilised for Fig. 9.

The LSA magmatism coincided with, or occurred sometime after, the final suturing of the Mongol-Okhotsk Ocean (e.g., Van der Voo et al., 2015; Wu et al., 2017). These samples have Y vs. Sr/Y values that trend into the adakite field (Fig. 6A) but plot with major- and trace-element concentrations unlike adakites (Fig. 10) and have geochemical resemblances to the Group 1 samples (e.g., Figs. 10, 12–14). We therefore interpret the LSA to have a source akin to the Group 1 lavas but have an adakite-like HREE depletion from late-stage fractionation of accessory minerals such as zircon and apatite (Fig. 7).

Despite the LSA attaining adakite-like HREE depletion via fractionation processes, the samples are more depleted in the HREEs at a given MgO or SiO_2 wt. % than the Group 1 lavas (e.g., Figs. 7 and 10). Furthermore, the LSA samples are more enriched in Na_2O than the Group 1 and 2 lavas (Fig. 10D) and have high Nb/Ta ratios (Fig. 12). We interpret these geochemical attributes to reflect a source modified by small-degree partial melts from a Mongol-Okhotsk slab.

The Group 2 lavas were compared to Mesozoic lavas from the Gobi Altai by Sheldrick et al. (2018) and interpreted as melts from a subduction-enriched preconditioned subcontinental lithospheric mantle (SCLM). The Group 1 lavas have similar geochemical characteristics, with a depletion in some HFSE (Nb, Ta and Ti) and have comparable Sr and Nd isotope signatures (Fig. 13). We therefore interpret the Group 1 basaltic-trachyandesite and trachyandesite lavas to be derived from the SCLM and suggest that this mantle underwent metasomatism from processes associated with the closure of the Mongol-Okhotsk Ocean. The single trachyte sample

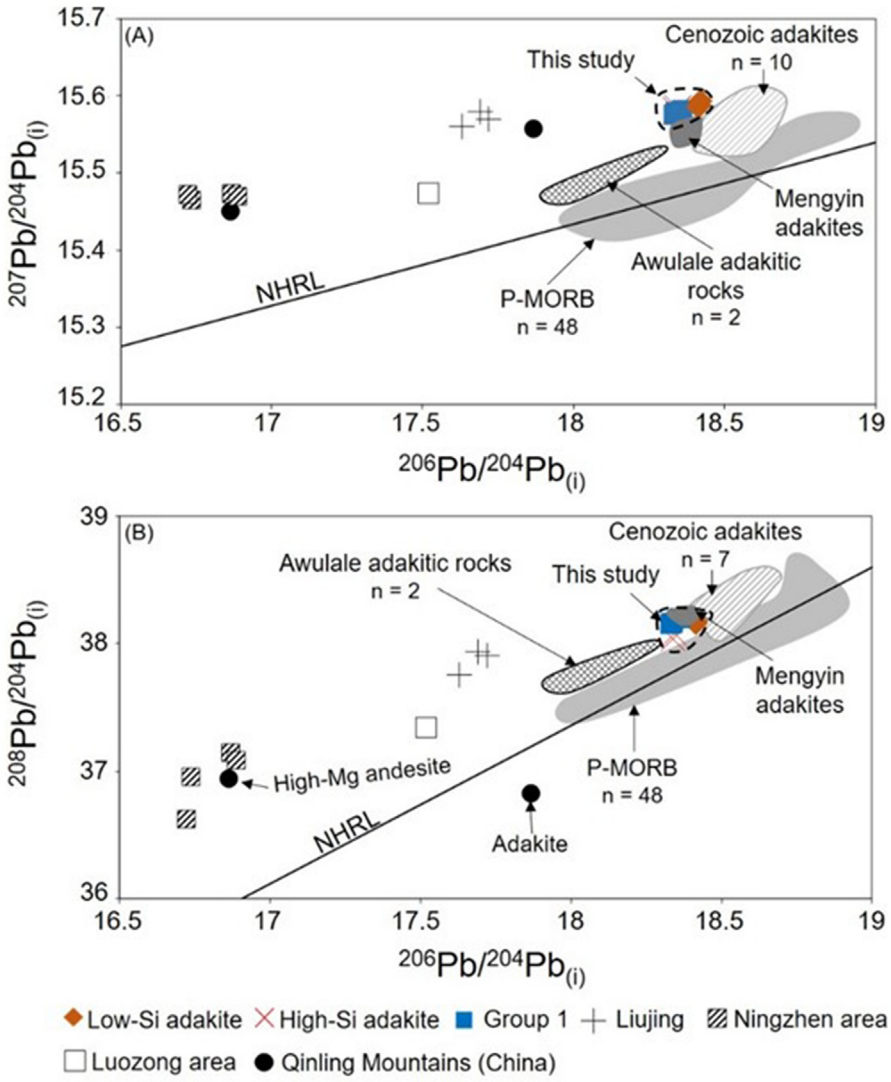

Fig. 14. (A) Plot of $^{206}Pb/^{204}Pb_{(i)}$ vs. $^{207}Pb/^{204}Pb_{(i)}$ and (B) a plot of $^{208}Pb/^{204}Pb_{(i)}$ vs. $^{206}Pb/^{204}Pb_{(i)}$. The adakites from Mengyin (China) and adakitic rocks from Liujing (China) are age corrected to 131 Ma (Wang et al., 2016). The high-Mg andesite and adakite (Qinling Mountains, China) from Xu et al. (2000). The Ningzhen area (China) adakitic samples are age corrected to 123 Ma (Xu et al., 2002). The Luozong area (China) adakitic samples are age corrected to 136 Ma (Wang et al., 2006). The Awulale adakitic rocks are age corrected to 260 Ma (Zhao et al., 2008; n = 2). The Cenozoic adakites field generated from: the Andean-Austral volcanic zone (Stern and Kilian, 1996; Lautaro, Viedma, Reclus and Mt. Burney); Cerro Pampa, South southern America (Kay et al., 1993) and Vizcaino Peninsula, Mexico (Aguillón-Robles et al., 2001.). The Pacific MORB field generated from: Juan de Fuca; Gorda; and East Pacific Rise (White et al., 1987; n = 48). Symbols are the same as in Fig. 13.

plots separately from Group 1 samples (Fig. 7) and it's unclear whether this sample reflects extensive magmatic differentiation (with later stage crustal contamination), from a source like the Group 1 samples – or whether this trachyte reflects a different melting/petrogenesis process.

Overall, the proximity of the adakites to the Mongol-Okhotsk suture is best explained by the involvement of a southward-subducting Mongol-Okhotsk slab. When this interpretation is combined with previous evidence for northwards-subduction of a Mongol-Okhotsk slab (Zorin, 1999; Van der Voo et al., 1999; Fritzell et al., 2016) it indicates the Mongol-Okhotsk Ocean closed in a bimodal fashion.

10. Conclusions

(1) Two alternative hypotheses are proposed to explain the HSA magmatism: (i) a southward-subducting Mongol-Okhotsk slab underwent partial melting in the Triassic during the closure of the Mongol-Okhotsk Ocean, with the resultant melts assimilating mantle and crustal material. Alternatively, (ii) basaltic underplating of a thickened (>50 km; >1.5 GPa), eclogite lower crust, foundered into the underlying mantle, and these crustal melts were then assimilated with minor mantle material, and eventually underwent crustal contamination.

(2) The LSA magmatism coincided with, or occurred shortly after, the final suturing of the Mongol-Okhotsk Ocean, and is proximal to the Mongol-Okhotsk suture. These melts are likely derived from a source modified by melts from a southward-subducted Mongol-Okhotsk slab. However, the LSA developed adakite-like HREE depletion from fractionation of late-stage accessory minerals.

(3) The Group 1 and 2 samples are derived from the SCLM; this mantle likely underwent metasomatism from processes associated with the closure of the Mongol-Okhotsk Ocean.

Acknowledgments

The analyses were supported by NERC grant IP-1610-0516. Thanks to Mungunshagai for providing field assistance.

Appendix A. Supplementary data

Supplementary data to this article can be found online at https://doi.org/10.1016/j.gr.2019.09.007.

References

Aguillón-Robles, A., Calmus, T., Benoit, M., Bellon, H., Maury, R.C., Cotten, J., Bourgois, J., Michaud, F., 2001. Late miocene adakites and Nb-enriched basalts from Vizcaino Peninsula, Mexico: indicators of East pacific Rise subduction below southern Baja California? Geology 29 (6), 531–534.
Atherton, M.P., Petford, N., 1993. Generation of sodium-rich magmas from newly underplated basaltic crust. Nature 362 (6416), 144.
Badarch, G., 2005. Tectonic overview of Mongolia. Mongolian Geosci. 27, 1–7.
Badarch, G., Cunningham, W.D., Windley, B.F., 2002. A new terrane subdivision for Mongolia: implications for the Phanerozoic crustal growth of Central Asia. J. Asian Earth Sci. 21 (1), 87–110.
Barry, T.L., Saunders, A.D., Kempton, P.D., Windley, B.F., Pringle, M.S., Dorjnamjaa, D., Saandar, S., 2003. Petrogenesis of Cenozoic basalts from Mongolia: evidence for the role of asthenospheric versus metasomatized lithospheric mantle sources. J. Petrol. 44 (1), 55–91.
Barry, T.L., Davies, J.H., Wolstencroft, M., Millar, I.L., Zhao, Z., Jian, P., Safonova, I., Price, M., 2017. Whole-mantle convection with tectonic plates preserves long-term global patterns of upper mantle geochemistry. Sci. Rep. 7 (1), 1870.
Bars, A., Miao, L., Fochin, Z., Baatar, M., Anaad, C., Togtokh, K., 2018. Petrogenesis and tectonic implication of the Late Mesozoic volcanic rocks in East Mongolia. Geol. J.
Batkhishig, B., Noriyoshi, T., Greg, B., 2010. Magmatism of the shuteen complex and carboniferous subduction of the gurvansaikhan terrane, south Mongolia. J. Asian Earth Sci. 37 (5–6), 399–411.
Bryant, J.A., Yogodzinski, G.M., Churikova, T.G., 2011. High-Mg# andesitic lavas of the Shisheisky Complex, Northern Kamchatka: implications for primitive calc-alkaline magmatism. Contrib. Mineral. Petrol. 161 (5), 791–810.
Bussien, D., Gombojav, N., Winkler, W., Von Quadt, A., 2011. The Mongol–Okhotsk Belt in Mongolia—an appraisal of the geodynamic development by the study of sandstone provenance and detrital zircons. Tectonophysics 510 (1–2), 132–150.
Castillo, Paterno R., 2006. An overview of adakite petrogenesis. Chin. Sci. Bull. 51 (3), 257–268.
Chen, B., Jahn, B.M., Tian, W., 2009. Evolution of the Solonker suture zone: constraints from zircon U–Pb ages, Hf isotopic ratios and whole-rock Nd–Sr isotope compositions of subduction-and collision-related magmas and forearc sediments. J. Asian Earth Sci. 34 (3), 245–257.
Chen, B., Jahn, B.M., Suzuki, K., 2013. Petrological and Nd-Sr-Os isotopic constraints on the origin of high-Mg adakitic rocks from the North China Craton: tectonic implications. Geology 41 (1), 91–94.
Cocks, L.R.M., Torsvik, T.H., 2007. Siberia, the wandering northern terrane, and its changing geography through the Palaeozoic. Earth Sci. Rev. 82 (1–2), 29–74.
Condie, K.C., 2005. TTGs and adakites: are they both slab melts? Lithos 80 (1–4), 33–44.
Dai, M., Yan, G., Liu, C., Deng, J., Li, Y., Jia, W., Lai, C.K., 2019. Southward subduction of the Mongolia–okhostk ocean: insights from early–middle triassic intrusive rocks from the jiawula–tsagenbulagen area in NE China. Geol. J.
Dash, B., Yin, A., Jiang, N., Tseveendorj, B., Han, B., 2015. Petrology, structural setting, timing, and geochemistry of Cretaceous volcanic rocks in eastern Mongolia: constraints on their tectonic origin. Gondwana Res. 27 (1), 281–299.
Davidson, J., Turner, S., Plank, T., 2012. Dy/Dy*: variations arising from mantle sources and petrogenetic processes. J. Petrol. 54 (3), 525–537.
Defant, M.J., Drummond, M.S., 1990. Derivation of some modern arc magmas by melting of young subducted lithosphere. Nature 347 (6294), 662.
Defant, M.J., Richerson, P.M., De Boer, J.Z., Stewart, R.H., Maury, R.C., Bellon, H., Drummond, M.S., Feigenson, M.D., Jackson, T.E., 1991. Dacite genesis via both slab melting and differentiation: petrogenesis of La Yeguada volcanic complex, Panama. J. Petrol. 32 (6), 1101–1142.
Deng, C., Sun, D., Li, G., Lu, S., Tang, Z., Gou, J., Yang, Y., 2019. Early cretaceous volcanic rocks in the Great xing'an range: late effect of a flat-slab subduction. J. Geodyn.
DePaolo, D.J., 1981. Trace element and isotopic effects of combined wallrock assimilation and fractional crystallisation. Earth Planet. Sci. Lett. 53 (2), 189–202.
Ewart, A., 1983. The mineralogy and petrology of Tertiary-Recent orogenic volcanic rocks: with special reference to the andesitic-basaltic compositional range. Andesites, pp. 25–87.
Foley, S.F., Barth, M.G., Jenner, G.A., 2000. Rutile/melt partition coefficients for trace elements and an assessment of the influence of rutile on the trace element characteristics of subduction zone magmas. Geochem. Cosmochim. Acta 64 (5), 933–938.
Foley, S., Tiepolo, M., Vannucci, R., 2002. Growth of early continental crust controlled by melting of amphibolite in subduction zones. Nature 417 (6891), 837.
Fritzell, E.H., Bull, A.L., Shephard, G.E., 2016. Closure of the Mongol–Okhotsk ocean: insights from seismic tomography and numerical modelling. Earth Planet. Sci. Lett. 445, 1–12.
Fujimaki, H., 1986. Partition coefficients of Hf, Zr, and REE between zircon, apatite, and liquid. Contrib. Mineral. Petrol. 94 (1), 42–45.
Gale, A., Dalton, C.A., Langmuir, C.H., Su, Y., Schilling, J.G., 2013. The mean composition of ocean ridge basalts. Geochem. Geophys. Geosyst. 14 (3), 489–518.
Gan, C., Wang, Y., Zhang, Y., Chen, X., 2019. Late jurassic magmatism in the interior south China block and its implication. J. Geol. Soc.
Gao, S., Rudnick, R.L., Carlson, R.W., McDonough, W.F., Liu, Y.S., 2002. Re–Os evidence for replacement of ancient mantle lithosphere beneath the North China craton. Earth Planet. Sci. Lett. 198 (3), 307–322.
Gao, S., Rudnick, R.L., Yuan, H.L., Liu, X.M., Liu, Y.S., Xu, W.L., Ling, W.L., Ayers, J., Wang, X.C., Wang, Q.H., 2004. Recycling lower continental crust in the North China craton. Nature 432 (7019), 892–897.
Halim, N., Kravchinsky, V., Gilder, S., Cogné, J.P., Alexyutin, M., Sorokin, A., Courtillot, V., Chen, Y., 1998. A palaeomagnetic study from the Mongol–Okhotsk region: rotated Early Cretaceous volcanics and remagnetized Mesozoic sediments. Earth Planet. Sci. Lett. 159 (3), 133–145.
Hansen, J., Skjerlie, K.P., Pedersen, R.B., De La Rosa, J., 2002. Crustal melting in the lower parts of island arcs: an example from the Bremanger Granitoid Complex, west Norwegian Caledonides. Contrib. Mineral. Petrol. 143 (3), 316–335.
Hastie, A.R., Kerr, A.C., Pearce, J.A., Mitchell, S.F., 2007. Classification of altered volcanic island arc rocks using immobile trace elements: development of the Th–Co discrimination diagram. J. Petrol. 48 (12), 2341–2357.
He, L., 2014. Numerical modeling of convective erosion and peridotite-melt interaction in big mantle wedge: implications for the destruction of the North China Craton. J. Geophys. Res.: Solid Earth 119 (4), 3662–3677.
He, L., 2015. Thermal regime of the north China craton: implications for craton destruction. Earth Sci. Rev. 140, 14–26.
Hofmann, A.W., 1988. Chemical differentiation of the Earth: the relationship between mantle, continental crust, and oceanic crust. Earth Planet. Sci. Lett. 90 (3), 297–314.
Irvine, T.N.J., Baragar, W.R.A.F., 1971. A guide to the chemical classification of the common volcanic rocks. Can. J. Earth Sci. 8 (5), 523–548.
Johnson, Cari L., Greene, Todd J., Zinniker, David A., Moldowan, J. Michael, Hendrix, Marc S., Carroll, Alan R., 2003. Geochemical characteristics and correlation of oil and nonmarine source rocks from Mongolia. AAPG Bull. 87 (5), 817–846.
Kamber, B.S., Collerson, K.D., 2000. Role of 'hidden'deeply subducted slabs in mantle depletion. Chem. Geol. 166 (3–4), 241–254.
Kay, S.M., Ramos, V.A., Marquez, M., 1993. Evidence in Cerro Pampa volcanic rocks for slab-melting prior to ridge-trench collision in southern South America. J. Geol. 101 (6), 703–714.
Kelemen, P.B., Hanghøj, K., Greene, A.R., 2003. One view of the geochemistry of subduction-related magmatic arcs, with an emphasis on primitive andesite and lower crust. Treatise Geochem. 3, 659.
Kelty, T.K., Yin, A., Dash, B., Gehrels, G.E., Ribeiro, A.E., 2008. Detrital-zircon geochronology of Paleozoic sedimentary rocks in the Hangay–Hentey basin, north-central Mongolia: implications for the tectonic evolution of the Mongol–Okhotsk Ocean in central Asia. Tectonophysics 451 (1–4), 290–311.
Kravchinsky, V.A., Cogné, J.P., Harbert, W.P., Kuzmin, M.I., 2002. Evolution of the Mongol-Okhotsk Ocean as constrained by new palaeomagnetic data from the Mongol-Okhotsk suture zone, Siberia. Geophys. J. Int. 148 (1), 34–57.
Liang, J.L., Ding, X., Sun, X.M., Zhang, Z.M., Zhang, H., Sun, W.D., 2009. Nb/Ta fractionation observed in eclogites from the Chinese continental scientific drilling project. Chem. Geol. 268 (1–2), 27–40.
Liang, C., Liu, Y., Zheng, C., Li, W., Neubauer, F., Zhang, Q., Zhang, D., 2019. Deformation patterns and timing of the thrust-nappe structures in the mohe formation in mohe basin, northeast China: implication of the closure timing of Mongol–Okhotsk ocean. Geol. J. 54 (2), 746–769.
Liu, S., Hu, R.Z., Gao, S., Feng, C.X., Zhong, H., Qi, Y., Wang, T., Qi, L., Feng, G., 2008. K-Ar ages and geochemical+ Sr-Nd isotopic compositions of adakitic volcanic rocks, western Shandong Province, eastern China: foundering of the lower continental crust. Int. Geol. Rev. 50 (8), 763–779.
Liu, H., Li, Y., He, H., Huangfu, P., Liu, Y., 2018. Two-phase southward subduction of the Mongol-Okhotsk oceanic plate constrained by Permian-Jurassic granitoids in the Erguna and Xing'an massifs (NE China). Lithos 304, 347–361.
Luhr, J.F., Carmichael, I.S., Varekamp, J.C., 1984. The 1982 eruptions of El Chichón Volcano, Chiapas, Mexico: mineralogy and petrology of the anhydrite-bearing pumices. J. Volcanol. Geotherm. Res. 23 (1–2), 69–108.
McDonough, W.F., Sun, S.S., 1995. The composition of the Earth. Chem. Geol. 120 (3–4), 223–253.
Meng, Q.R., 2003. What drove late Mesozoic extension of the northern China–Mongolia tract? Tectonophysics 369 (3–4), 155–174.
Menzies, M., Xu, Y., Zhang, H., Fan, W., 2007. Integration of geology, geophysics and geochemistry: a key to understanding the North China Craton. Lithos 96 (1–2), 1–21.
Moyen, J.F., 2009. High Sr/Y and La/Yb ratios: the meaning of the "adakitic signature". Lithos 112 (3–4), 556–574.
Rapp, R.P., Watson, E.B., 1995. Dehydration melting of metabasalt at 8–32 kbar: implications for continental growth and crust-mantle recycling. J. Petrol. 36 (4), 891–931.

Rapp, R.P., Watson, E.B., Miller, C.F., 1991. Partial melting of amphibolite/eclogite and the origin of Archean trondhjemites and tonalites. Precambrian Res. 51 (1–4), 1–25.
Rapp, R.P., Shimizu, N., Norman, M.D., Applegate, G.S., 1999. Reaction between slab-derived melts and peridotite in the mantle wedge: experimental constraints at 3.8 GPa. Chem. Geol. 160 (4), 335–356.
Rippington, S., Cunningham, D., England, R., 2008. Structure and petrology of the altan Uul ophiolite: new evidence for a late carboniferous suture in the Gobi Altai, southern Mongolia. J. Geol. Soc. 165 (3), 711–723.
Rippington, S., Cunningham, D., England, R., Hendriks, B., 2013. The crustal assembly of southern Mongolia: new structural, lithological and geochronological data from the Nemegt and Altan ranges. Gondwana Res. 23 (4), 1535–1553.
Rudnick, R.L., Fountain, D.M., 1995. Nature and composition of the continental crust: a lower crustal perspective. Rev. Geophys. 33 (3), 267–309.
Rudnick, R.L., Gao, S., 2003. Composition of the continental crust. Treatise Geochem. 3, 659.
Ruppen, D., Knaf, A., Bussien, D., Winkler, W., Chimedtseren, A., von Quadt, A., 2014. Restoring the Silurian to Carboniferous northern active continental margin of the Mongol–Okhotsk Ocean in Mongolia: Hangay-Hentey accretionary wedge and seamount collision. Gondwana Res. 25 (4), 1517–1534.
Safonova, Inna, 2017. Juvenile versus recycled crust in the Central Asian Orogenic Belt: implications from ocean plate stratigraphy, blueschist belts and intra-oceanic arcs. Gondwana Res. 47, 6–27.
Safonova, I.Y., Santosh, M., 2014. Accretionary complexes in the Asia-Pacific region: tracing archives of ocean plate stratigraphy and tracking mantle plumes. Gondwana Res. 25 (1), 126–158.
Sen, C., Dunn, T., 1994. Dehydration melting of a basaltic composition amphibolite at 1.5 and 2.0 GPa: implications for the origin of adakites. Contrib. Mineral. Petrol. 117 (4), 394–409.
Sengör, A.C., Natal'In, B.A., 1996. Turkic-type orogeny and its role in the making of the continental crust. Annu. Rev. Earth Planet Sci. 24 (1), 263–337.
Şengör, A.M.C., Natal'In, B.A., Burtman, V.S., 1993. Evolution of the Altaid tectonic collage and Palaeozoic crustal growth in Eurasia. Nature 364 (6435), 299.
Seton, M., Müller, R.D., Zahirovic, S., Gaina, C., Torsvik, T., Shephard, G., Talsma, A., Gurnis, M., Turner, M., Maus, S., Chandler, M., 2012. Global continental and ocean basin reconstructions since 200 Ma. Earth Sci. Rev. 113 (3–4), 212–270.
Sheldrick, T.C., Barry, T.L., Van Hinsbergen, D.J., Kempton, P.D., 2018. Constraining lithospheric removal and asthenospheric input to melts in Central Asia: a geochemical study of Triassic to Cretaceous magmatic rocks in the Gobi Altai (Mongolia). Lithos 296, 297–315.
Stern, C.R., Kilian, R., 1996. Role of the subducted slab, mantle wedge and continental crust in the generation of adakites from the Andean Austral Volcanic Zone. Contrib. Mineral. Petrol. 123 (3), 263–281.
Sun, S.S., McDonough, W.S., 1989. Chemical and isotopic systematics of oceanic basalts: implications for mantle composition and processes. Geol. Soc. London Spec. Publ. 42 (1), 313–345.
Tang, J., Xu, W.L., Wang, F., Wang, W., Xu, M.J., Zhang, Y.H., 2014. Geochronology and geochemistry of early–middle triassic magmatism in the erguna massif, NE China: constraints on the tectonic evolution of the Mongol–Okhotsk ocean. Lithos 184, 1–16.
Tang, J., Xu, W., Wang, F., Ge, W., 2018. Subduction history of the paleo-pacific slab beneath eurasian continent: mesozoic-paleogene magmatic records in north-east Asia. Sci. China Earth Sci. 61, 527–559.
Tomurtogoo, O., et al., 1999. Geological map of Mongolia 1:1000,000. In: Mongolian Academy of Sciences, Institute of Geology and Mineral Resources, Mineral Resources Authority of Mongolia.
Tomurtogoo, O., Windley, B.F., Kröner, A., Badarch, G., Liu, D.Y., 2005. Zircon age and occurrence of the Adaatsag ophiolite and Muron shear zone, central Mongolia: constraints on the evolution of the Mongol–Okhotsk ocean, suture and orogen. J. Geol. Soc. 162 (1), 125–134.
Torsvik, T.H., Cocks, L.R.M., 2016. Earth History and Palaeogeography. Cambridge University Press.
Van der Voo, R., Spakman, W., Bijwaard, H., 1999. Mesozoic subducted slabs under Siberia. Nature 397 (6716), 246.
Van der Voo, R., van Hinsbergen, D.J., Domeier, M., Spakman, W., Torsvik, T.H., 2015. Latest Jurassic–earliest Cretaceous closure of the Mongol-Okhotsk Ocean: a paleomagnetic and seismological-tomographic analysis. Geol. Soc. Am. Spec. Pap. 513, 589–606.
Van Hinsbergen, D.J., Cunningham, D., Straathof, G.B., Ganerød, M., Hendriks, B.W., Dijkstra, A.H., 2015. Triassic to Cenozoic multi-stage intra-plate deformation focused near the Bogd Fault system, Gobi Altai, Mongolia. Geosci. Front. 6 (5), 723–740.
Vervoort, J.D., Patchett, P.J., Blichert-Toft, J., Albarède, F., 1999. Relationships between Lu–Hf and Sm–Nd isotopic systems in the global sedimentary system. Earth Planet. Sci. Lett. 168 (1), 79–99.
Wang, F., Zhou, X.H., Zhang, L.C., Ying, J.F., Zhang, Y.T., Wu, F.Y., Zhu, R.X., 2006. Late mesozoic volcanism in the Great xing'an range (NE China): timing and implications for the dynamic setting of NE Asia. Earth Planet. Sci. Lett. 251 (1), 179–198.
Wang, W., Tang, J., Xu, W.L., Wang, F., 2015. Geochronology and geochemistry of Early Jurassic volcanic rocks in the Erguna Massif, northeast China: petrogenesis and implications for the tectonic evolution of the Mongol–Okhotsk suture belt. Lithos 218, 73–86.
Wang, H., Xu, Z., Lu, X., Fu, B., Lu, J., Yang, X., Zhao, Z., 2016. Two-types of Early Cretaceous adakitic porphyries from the Luxi terrane, eastern North China Block: melting of subducted Paleo-Pacific slab and delaminated newly underplated lower crust. Lithos 240, 140–154.
Winchester, J.A., Floyd, P.A., 1977. Geochemical discrimination of different magma series and their differentiation products using immobile elements. Chem. Geol. 20, 325–343.
Windley, B.F., Alexeiev, D., Xiao, W., Kröner, A., Badarch, G., 2007. Tectonic models for accretion of the central asian orogenic belt. J. Geol. Soc. 164 (1), 31–47.
Windley, B.F., Maruyama, S., Xiao, W.J., 2010. Delamination/thinning of sub-continental lithospheric mantle under Eastern China: the role of water and multiple subduction. Am. J. Sci. 310 (10), 1250–1293.
Winther, K.T., 1996. An experimentally based model for the origin of tonalitic and trondhjemitic melts. Chem. Geol. 127 (1–3), 43–59.
Wolf, M.B., Wyllie, P.J., 1994. Dehydration-melting of amphibolite at 10 kbar: the effects of temperature and time. Contrib. Mineral. Petrol. 115 (4), 369–383.
Wu, L., Kravchinsky, V.A., Gu, Y.J., Potter, D.K., 2017. Absolute reconstruction of the closing of the Mongol-Okhotsk Ocean in the Mesozoic elucidates the genesis of the slab geometry underneath Eurasia. J. Geophys. Res.: Solid Earth 122 (7), 4831–4851.
Xiao, Wenjiao, Windley, Brian F., Sun, Shu, Li, Jiliang, Huang, Baochun, Chunming, Han, Chao, Yuan, Min, Sun, Hanlin, Chen, 2015. A tale of amalgamation of three permo-triassic collage systems in central Asia: oroclines, sutures, and terminal accretion. Annu. Rev. Earth Planet Sci. 43, 477–507.
Xiong, X.L., Li, X.H., Xu, J.F., Li, W.X., Zhao, Z.H., Wang, Q., Chen, X.M., 2003. Extremely high-Na adakite-like magmas derived from alkali-rich basaltic underplate: the Late Cretaceous Zhantang andesites in the Huichang Basin, SE China. Geochem. J. 37 (2), 233–252.
Xiong, X.L., Adam, J., Green, T.H., 2005. Rutile stability and rutile/melt HFSE partitioning during partial melting of hydrous basalt: implications for TTG genesis. Chem. Geol. 218 (3–4), 339–359.
Xiong, X., Keppler, H., Audétat, A., Ni, H., Sun, W., Li, Y., 2011. Partitioning of Nb and Ta between rutile and felsic melt and the fractionation of Nb/Ta during partial melting of hydrous metabasalt. Geochem. Cosmochim. Acta 75 (7), 1673–1692.
Xu, J.F., Wang, Q., Yu, X.Y., 2000. Geochemistry of high-Mg andesites and adakitic andesite from the Sanchazi block of the Mian-Lue ophiolitic melange in the Qinling Mountains, central China: evidence of partial melting of the subducted Paleo-Tethyan crust. Geochem. J. 34 (5), 359–377.
Xu, J.F., Shinjo, R., Defant, M.J., Wang, Q., Rapp, R.P., 2002. Origin of Mesozoic adakitic intrusive rocks in the Ningzhen area of east China: partial melting of delaminated lower continental crust? Geology 30 (12), 1111–1114.
Zhang, K.J., 2014. Genesis of the late mesozoic Great xing'an range large igneous province in eastern central Asia: a mongol–okhotsk slab window model. Int. Geol. Rev. 56 (13), 1557–1583.
Zhang, H.F., Sun, M., Zhou, X.H., Fan, W.M., Zhai, M.G., Yin, J.F., 2002. Mesozoic lithosphere destruction beneath the North China Craton: evidence from major-, trace-element and Sr–Nd–Pb isotope studies of Fangcheng basalts. Contrib. Mineral. Petrol. 144 (2), 241–254.
Zhang, H.F., Sun, M., Zhou, X.H., Ying, J.F., 2005. Geochemical constraints on the origin of Mesozoic alkaline intrusive complexes from the North China Craton and tectonic implications. Lithos 81 (1–4), 297–317.
Zhao, Z.H., Xiong, X.L., Wang, Q., Wyman, D.A., Bao, Z.W., Bai, Z.H., Qiao, Y.L., 2008. Underplating-related adakites in Xinjiang tianshan, China. Lithos 102 (1), 374–391.
Zhao, C., Qin, K.Z., Song, G.X., Li, G.M., 2019. Switch of geodynamic setting from the Paleo-Asian Ocean to the Mongol-Okhotsk ocean: evidence from granitoids in the Duobaoshan ore field, heilongjiang province, northeast China. Lithos 336, 202–220.
Zhou, J.B., Wilde, S.A., 2013. The crustal accretion history and tectonic evolution of the NE China segment of the Central Asian Orogenic Belt. Gondwana Res. 23 (4), 1365–1377.
Zhou, J.B., Wilde, S.A., Zhao, G.C., Zhang, X.Z., Wang, H., Zeng, W.S., 2010. Was the easternmost segment of the central asian orogenic belt derived from gondwana or Siberia: an intriguing dilemma? J. Geodyn. 50 (3–4), 300–317.
Zindler, A., Hart, S., 1986. Chemical geodynamics. Annu. Rev. Earth Planet Sci. 14 (1), 493–571.
Zonenshain, L.P., 1990. Geology of the USSR: a plate tectonic synthesis. Geodyn. Monograph 21, 242.
Zorin, Y.A., 1999. Geodynamics of the western part of the Mongolia–Okhotsk collisional belt, Trans-Baikal region (Russia) and Mongolia. Tectonophysics 306 (1), 33–56.